

Constraining the Interiors of Asteroids Through Close Encounters

Jack T. Dinsmore,^{1*} Julien de Wit²

¹*Department of Physics, Massachusetts Institute of Technology*

²*Department of Earth, Atmospheric, and Planetary Science, Massachusetts Institute of Technology*

Accepted XXX. Received YYY; in original form ZZZ

ABSTRACT

Knowledge of the interior distribution of an asteroid can reveal its composition and constrain its evolutionary history. However, most observations are not sensitive to interior structure. We investigate the degree to which asteroid interior density distributions can be extracted from rotational velocity data gathered during a close encounter. We derive the equations of motion for a rigid asteroid’s orientation and angular velocity to arbitrary order and use them to generate synthetic rotational velocity data for a representative asteroid on a close Earth encounter. Using Markov Chain Monte Carlo fits, we re-extract the density moments of the asteroid in a wide range of scenarios to measure the degree to which best-fitting parameter precision is affected. Specifically, we use many injection-retrieval tests to study fit precision’s dependence on the asteroid’s moment of inertia, observational precision and cadence, orbital parameters, and initial spin pole direction as well as the quantity of near-pericentre data and the central body oblateness. Finally, we discuss the degeneracy between the density moments and the actual density distribution and propose three models to construct a representative density distribution from fit results.

Key words: minor planets, asteroids: general – methods: data analysis

1 INTRODUCTION

Over the past twenty years, the increase in quantity and quality of sensitive all-sky surveys has prompted the discovery of numerous asteroids. Such advances have been made via ground-based surveys such as the Catalina Sky Survey [Larson et al. \(1998\)](#), Pan-STARRS [Kaiser et al. \(2002\)](#), and the Lincoln Near-Earth Asteroid Research project (LINEAR) [Stokes et al. \(2000\)](#), as well as space-based instruments such as the Wide-field Infrared Survey Explorer (WISE) mission [Wright et al. \(2010\)](#). Many of these asteroids are relatively small, but some are kilometre-sized and a few are predicted to encounter Earth or other planets closely in the near future. More encounter candidates are likely to be discovered in the future — for Earth or other planets — potentially by the Large-aperture Synoptic Survey Telescope (LSST) or global telescope networks such as the Las Cumbres Observatory (LCO). Light curve analysis has been performed on many of these new asteroids to study their surface properties, but observations that are sensitive to the interior structure of the asteroid are rarer.

However, tidal torque acting on an asteroid and perturbing its angular velocity during an encounter presents

an opportunity to constrain the asteroid mass distribution. Such angular velocity perturbations have been observed and used to extract asteroid properties in several cases, including for the 2013 encounter of (367943) Duende with Earth [Moskovitz et al. \(2020\)](#); [Benson et al. \(2020\)](#), and asteroid binaries (3905) Doppler and (617) Patroclus respectively. Altered rotational states altered by Solar tidal torque have been excluded for 1I/2017 U1 ‘Oumuamua [Kwiecinski et al. \(2018\)](#).

The upcoming encounter of Apophis is of particular interest and much theoretical work has been devoted to accurate estimates of its orbital and physical properties, and predictions of how its angular velocity will be affected by tidal torque [Yu et al. \(2014\)](#); [Hirabayashi et al. \(2021\)](#); [Valvano et al. \(2022\)](#); [Lee et al. \(2022\)](#); [Souchay et al. \(2014, 2018\)](#). This research builds on a larger body of theoretical work showing that the tidal torque, observed through angular velocity perturbations, is sensitive to asteroid interior density distribution [Naidu & Margot \(2015\)](#); [Makarov et al. \(2022\)](#); [Richardson et al. \(1998\)](#); [Scheeres et al. \(2004\)](#). This two-body generalized system has been studied to different orders and with several different methods [Paul \(1988\)](#); [Scheeres et al. \(2000\)](#); [Ashenberg \(2007\)](#); [Boué & Laskar \(2009\)](#); [Hou et al. \(2017\)](#). The success of this work is demonstrated by the recent extraction of moment of inertia ratios

* E-mail: jtdinsmo@mit.edu

for Duende [Moskovitz et al. \(2020\)](#). However, density distribution information beyond the moment of inertia ratios have not yet been extracted for planetary encounters. More research is needed to study in what cases these effects are observable, and what factors generally inhibit observation of these sub-dominant terms.

In this paper, we address this question by deriving a new equation of motion for an asteroid encounter system, using , and describe a simulation used to integrate the equation of motion and produce synthetic data of angular velocity over time (section 2.1).it to simulate a generic asteroid encounter of Earth. In section 2, we then extract physical characteristics of the asteroid (specifically, density moments) from synthetic data via a Markov Chain Monte Carlo (MCMC) fit. We also describe methods to extract estimates of density distribution from these density moments. In section 3, we demonstrate our fit process and evaluate our density distribution extraction methods on density moments extracted from fits to synthetic data. In section 4, we measure the uncertainties in the Posterior Probability Distribution (PPD) of density moments as a function of various encounter parameters such as the observational uncertainty, encounter orbital parameters, asteroid physical properties, and more.

2 METHODS

In appendix ??, we derive a novel equation for the tidal torque experienced by an asteroid in a two-body system, accurate to arbitrary order. The equation is written in terms of the asteroid “length”

$$a_{\mathcal{A}}^2 = \frac{1}{\mu_{\mathcal{A}}} \int_{\mathcal{A}} d^3 r \rho_{\mathcal{A}}(\mathbf{r}) r^2 \quad (1)$$

and (complex) “density moments”

$$K_{\ell m} = \frac{1}{\mu_{\mathcal{A}} a_{\mathcal{A}}^{\ell}} \int_{\mathcal{A}} d^3 r \rho_{\mathcal{A}}(\mathbf{r}) R_{\ell m}(\mathbf{r}), \quad (2)$$

both of which are constant and only need to be computed once to generate data. Here, $\rho_{\mathcal{A}}(\mathbf{r})$ is the asteroid density distribution, $\mu_{\mathcal{A}}$ is the asteroid mass, and $R_{\ell m}$ are the regular solid spherical harmonics (see the appendix for details). They produce a tidal torque of

$$\begin{aligned} \tau = & G \frac{\mu_{\mathcal{A}} \mu_{\mathcal{B}}}{2} \left[\sum_{\ell m} a_{\mathcal{B}}^{\ell} J_{\ell m} \sum_{\ell' m'} a_{\mathcal{A}}^{\ell'} S_{\ell+\ell', m+m'}^{*}(\mathbf{D}) (-1)^{\ell'} \right. \\ & \times \sum_{m''=-\ell'}^{\ell'} \sqrt{\frac{(\ell'-m'')!(\ell'+m'')!}{(\ell'-m')!(\ell'+m')!}} \mathcal{D}_{m'm''}^{\ell'}(\alpha, \beta, \gamma)^* \\ & \times \left. \left((i\hat{\mathbf{x}} - \hat{\mathbf{y}})(\ell' - m'' + 1) K_{\ell', m''-1} \right. \right. \\ & \left. \left. + (i\hat{\mathbf{x}} + \hat{\mathbf{y}})(\ell' + m'' + 1) K_{\ell', m''+1} + 2im''\hat{\mathbf{z}} K_{\ell'm''} \right) \right], \end{aligned} \quad (3)$$

where \mathbf{D} is the position of the asteroid; α , β , and γ are Euler angles expressing the orientation of the asteroid; and $\mu_{\mathcal{B}}$ and $J_{\ell m}$ are the mass and density moments of the central body respectively; and $S_{\ell m}$ are the irregular solid spherical harmonics.

In section 2.1, we describe the simulation used to integrate the equations of motion. In section 2.2, we define the

uncertainty model used to add noise to the data, and we describe how PPDs for density moments were extracted from spin-pole data in section 2.3. Finally, we outline a general model to extract density distributions from density moments in section 2.4 and define specific model implementations in section 2.5

2.1 Simulation design

We built a custom simulation in C++ to produce angular velocity data as a function of time. This simulation requires as initial data (1) the orbital parameters of the asteroid r_p (perigee distance) and v_{∞} (hyperbolic excess velocity); (2) the cadence of angular velocity observation Δt ; (3) the central body moments $J_{\ell m}$, mass $\mu_{\mathcal{B}}$, and radius $a_{\mathcal{B}}$; (4) the initial asteroid angular velocity in the inertial frame Ω_0 ; (5) the asteroid length $a_{\mathcal{A}}$; and (6) the asteroid’s density moments $K_{\ell m}$ and initial Euler angle γ_0 . All parameters except (6) are assumed to be known to high accuracy. One can imagine that $a_{\mathcal{A}}$ is approximated by light-curve analysis, but if not, it is still necessary to fix $a_{\mathcal{A}}$ or else the values of $K_{\ell m}$ are degenerate with $a_{\mathcal{A}}$.

We further assume that the asteroid is initially not tumbling. Thus, the rotational velocity is aligned with a principal axis (assumed to be $\hat{\mathbf{z}}$, which maximizes moment of inertia). This sets $\beta = 0$ and we can further choose $\alpha = 0$. Thus, only the Euler angle γ_0 is necessary to provide initial data for the simulation.

We begin our simulation at $D = 10r_p$, with velocity predicted by Kepler’s laws given by the orbital parameters. Since the leading order of the equations of motion is $\ell' = 2, \ell = 0$, this corresponds roughly to a torque of 10^{-3} times the maximum torque at perigee. Unless otherwise indicated, the simulation is terminated at $D = 10r_p$ as well.

With the simulation inputs specified, the equations of motion are integrated via the Runge-Kutta fourth order method, with a variable time step

$$dt = dt_{\min} + 10^{-3} (dt_{\max} - dt_{\min}) \left[\left(\frac{D}{r_p} \right)^3 - 1 \right]. \quad (4)$$

The parameters dt_{\max} and dt_{\min} (20 and 10 seconds respectively) were chosen such that the error was ~ 100 times the floating point error, and that neighbouring values of $K_{\ell m}$ yielded significantly different spin pole data compared to floating point error. The data used to choose this dt was obtained using the reference asteroid configuration, described in appendix ??.

2.2 Uncertainty model

To add noise to data generated via the above simulation, we use the following uncertainty model. Each asteroid spin vector Ω is assumed to be uncorrelated with other spin vectors, and we model uncertainty in the orientation and in the period as also uncorrelated. Consider a true spin vector Ω^* . For the sake of description, we work in coordinates in which $\Omega^* \parallel \hat{\mathbf{z}}$. Then, expressing the observed spin vector Ω in spherical coordinates, we draw the polar angle from a normal distribution with standard deviation σ_{θ} centred on zero and the azimuthal angle from a uniform distribution. We

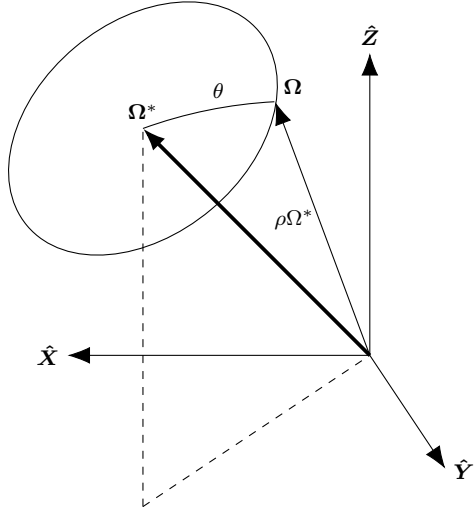


Figure 1. Diagram in the inertial frame of the uncertainty model used to define the probability that the true spin vector Ω^* should be observed as Ω . The parameter θ is drawn from a Gaussian with width σ_θ , and ρ is drawn from a log normal distribution with width σ_ρ .

also draw the ratio $\rho = \Omega/\Omega^*$ from a log-normal distribution centred on one, with width σ_ρ . We generally represent $\sigma_\theta > \sigma_\rho$ under the assumption that period is better constrained by light-curve data than spin pole. Explicitly, the probability density function (PDF) of ρ is

$$P(\rho) = \frac{1}{\rho\sqrt{2\pi\sigma_\rho^2}} \exp\left(-\frac{\ln^2 \rho}{2\sigma_\rho^2}\right). \quad (5)$$

See figure 1 for an illustration of the uncertainty model.

The log likelihood resulting from this uncertainty model is (excluding additive constants)

$$\ln \mathcal{L} = -\frac{1}{2} \sum_{i=0} \left[\frac{\cos^{-1}(\Omega_i^* \cdot \Omega_i / (\Omega_i^* \Omega_i))}{\sigma_\theta^2} + \frac{\ln(\Omega_i/\Omega_i^*)^2}{\sigma_\rho^2} + 2 \ln \frac{\Omega_i}{\Omega_i^*} \right]. \quad (6)$$

where Ω_i is the i th spin vector in the data set.

This model was chosen because it separates spin pole and period uncertainty. Therefore, if one is more precisely determined by measurement, σ_θ and σ_ρ can be adjusted separately in accordance.

2.3 Extracting density moments from spin data

Given synthetic data, an Affine Invariant Markov Chain Monte Carlo (MCMC) Ensemble sampler was used to generate PPDs from flat priors. We use the Python implementation `emcee` Foreman-Mackey et al. (2013). Our parameters were γ_0 , K_{20} , K_{22} , and K_{3m} (10 in total), and were bounded by $|\gamma_0| < \pi/4$, and bounds on K_{2m} given in equation ???. Note that γ_0 is degenerate with $\gamma_0 + \pi/2$ since this is equivalent to re-labeling \hat{y} as \hat{x} and \hat{x} as $-\hat{y}$. The other bounds were $|K_{3m}| < 1$.

The MCMC was determined to converge when the fractional change in autocorrelation time (computed every 100 iterations) was one percent, and the number of iterations

computed so far was more than 100 times the autocorrelation time. The MCMC fit also was set to terminate if more than 10^5 iterations were run, but this only occurred for fits in which the data was too low quality to resolve the parameters. 10^4 iterations was often sufficient, which generally consumed about 7 hours of computation time on a super computer running 16 threads on 8 cores.

Before the MCMC was run, local minima in the likelihood were found via the Nelder-Mead algorithm implemented in `scipy` Gao & Han (2012). It was found that only one local minimum existed, except when $K_{22} = 0$ in which case rotational symmetry caused multiple values of γ_0 to be degenerate. Walkers were initialized near this local minimum, distributed with probability distributed as a Gaussian approximation of the likelihood, as determined via the inverse Hessian of the likelihood at the minimum. Due to the high sensitivity of the angular velocity data to density moments, the minimization procedure sometimes failed to isolate the minimum likelihood. Therefore, a simpler simulation without the K_{3m} terms of equation 3 was first used to minimize likelihood as a function of γ_0 and K_{2m} , and then the full simulation was used to find K_{3m} , with γ_0 and K_{2m} fixed. This tiered minimization process motivates us to call γ_0 and K_{2m} the “first-order parameters” and K_{3m} the “second-order parameters.”

We further subdivided the minimization process by first minimizing with respect to data truncated at the point after perigee where $D = fr_p$ for some manually-set fraction f . In practice, $f = 2$ often led to success. The minimum was then further refined by minimizing based on the full data, with the previous minimum as the initial estimate.

2.4 Extracting density distributions from density moments: general model design

The asteroid density distribution $\rho_A(\mathbf{r})$ is not uniquely constrained via tidal torque interactions because only the density moments $K_{\ell m}$ contribute to equation 3. However, by making sufficient assumptions about the density distribution, we can nevertheless estimate $\rho(\mathbf{r})$ from $K_{\ell m}$. Here, we outline three different assumptions which constitute three models for extracting density distributions from density moments. One of them can be chosen, or another created, depending on what features are desired to be represented in the density distribution.

All three of these models assume that a_A and the asteroid shape is known (for example, by light curve or radar data). Uncertainty on this shape estimate is assumed to be small. The models then produce a density distribution $\rho_A(\mathbf{r})$ with uncertainty from $K_{\ell m}$ propagated to uncertainty in ρ_A . In section 3, we were forced to fix a_A rather than fit for it because a_A is degenerate with scaling the K_{3m} components. However, a_A contains information about the density distribution as shown by its definition in equation 1. It might therefore be unreasonable to assume that it is exactly determined by light-curve or radar analysis. If a_A is too uncertain to be used as a known quantity when extracting density distributions from the moments, then the following models are flexible enough that the a_A constraint can be removed. Likewise, if the asteroid shape is not known with certainty, a fourth model described in appendix ?? can be used to extract asteroid shape assuming constant density.

Note that, since the overall mass of the asteroid is not observable from tidal torque, we do not expect to measure ρ in an absolute sense. Only the differences in ρ across the body are measurable.

To set the shape of the asteroid, we assume that an indicator function $\mathbf{1}(\mathbf{r})$ has been determined such that $\mathbf{1}(\mathbf{r}) = 1$ inside the asteroid and 0 outside, where $\mathbf{1}(\mathbf{r})$ is defined in some frame whose orientation with respect to Earth is known. Since the asteroid rotates around its centre of mass during observations, we assume that the location of the centre of mass is also known in this frame, so that we can set it to be the origin.

We define a new coordinate system, the “hybrid frame,” which coincides exactly with body-fixed frame at the initial orientation of the asteroid assuming that the fit result for γ_0 is perfectly accurate. The orientation of the hybrid frame with respect to the inertial frame is therefore exactly known, so that $\mathbf{1}$ is also exact in the hybrid frame. The $K_{\ell m}$ components are known in the body-fixed frame which aligns with the hybrid frame up to uncertainty in γ_0 . We will solve for $\rho(\mathbf{r})$ in the hybrid frame given fit results $K_{\ell m}$ (known in the body-fixed frame) and the fixed a_A (equal in all frames).

The density moments defined in equation 2 are not linear in $\rho(\mathbf{r})$, but we may fix a_A at the value assumed during the fit, removing the non-linearity induced by division by a_A . Furthermore, since the system is independent of the total asteroid mass, we set μ_A equal to an arbitrary constant which makes equation 2 linear in $\rho(\mathbf{r})$. Similarly, the form of equation 1 guarantees that a_A^2 is linear in $\rho(\mathbf{r})$. Equation 1 and the $K_{00} = 1$ component of equation 2 can each be applied as constraints to enforce these choices of a_A^2 and μ_A .

Suppose that we restrict the number of degrees of freedom of $\rho(\mathbf{r})$ from infinity to m by explicitly defining some function $\rho(\mathbf{r}, \Theta)$ for an m -dimensional vector Θ which contains the free parameters of ρ . We will leave the explicit definition of $\rho(\mathbf{r}, \Theta)$ to the model descriptions below, but for now we assume that ρ is linear in Θ ; i.e.,

$$\rho(\mathbf{r}, \Theta) = \mathbf{B}(\mathbf{r}) \cdot \Theta \quad (7)$$

for a m -dimensional vector $\mathbf{B}(\mathbf{r})$. (\mathbf{B} need not be linear in \mathbf{r} .) Thus, the defining equations of a_A^2 and $K_{\ell m}$ are linear in Θ . We further assume that the model describes a way to reverse this equation, to write

$$\Theta = AK \quad (8)$$

where A is a matrix. Here, we have arranged a_A^2 and $K_{\ell m}$ into a vector K , which we say has n dimensions. The order of this arrangement is irrelevant, as long as it is kept consistent.

To propagate uncertainties from \mathbf{K} to Θ and therefore $\rho(\mathbf{r})$, we need the covariance matrix Σ_K for \mathbf{K} . First, assume that the hybrid frame is offset from the body-fixed frame by some small angle $\Delta\gamma$, which results from uncertainty in γ_0 . Then

$$K_{\ell m}^{\text{hybrid}} = e^{-im\Delta\gamma} K_{\ell m}^{\text{body-fixed}}. \quad (9)$$

by equation ???. Since $K_{\ell m}^{\text{body-fixed}}$ was obtained by an MCMC fit, a large set of PPD-distributed samples is available for $\Delta\gamma$ and $K_{\ell m}^{\text{body-fixed}}$, and the covariance matrix Σ_K can be computed statistically in the hybrid frame by applying equation 9 to the samples. Then, propagation of uncertainty guarantees that the covariance matrix of Θ is

$\Sigma_\Theta = A\Sigma_K A^T$ and the density distribution and uncertainty on density distribution are equal to

$$\rho(\mathbf{r}) = \mathbf{B}(\mathbf{r})^T AK \quad \sigma_\rho^2(\mathbf{r}) = \mathbf{B}(\mathbf{r})^T A\Sigma_K A^T \mathbf{B}(\mathbf{r}). \quad (10)$$

The purpose of a model is therefore to restrict the space of valid density distributions by defining the $m \times n$ -dimensional constant matrix A and the m -dimensional vector $\mathbf{B}(\mathbf{r})$ such that equations 8 and 7 are true. Then the density distribution and its uncertainty are given by equation 10.

2.5 Model implementations for extracting density distributions from density moments

In the following sections, three possible models for extracting density distributions from moments (i.e., choices of $\mathbf{B}(\mathbf{r})$ and A defined above) are given.

2.5.1 The “likelihood” model

A natural way to restrict the degrees of freedom of $\rho(\mathbf{r})$ is by defining a likelihood function \mathcal{L} on the density distribution and choosing the one distribution which maximizes likelihood and exactly reproduces \mathbf{K} . We call this method the “likelihood” model. This likelihood should not be confused with the likelihood of equation 6, which was a function of the spin data, not the density distribution. The choice of the density \mathcal{L} is arbitrary, but the linearity of the model design outlined in the previous section will require a Gaussian likelihood.

To employ this likelihood method, we divide the asteroid into a square grid of $m \gg n$ elements, each of which is assumed to have uniform density $\rho_0 + \Theta_i$, where ρ_0 is constant across the asteroid and Θ_i is a local deviation. This defines the model function $\mathbf{B}(\mathbf{r})$, which is zeroed in all components except for the i th, where i is the index of the grid element that contains \mathbf{r} .

We use a likelihood of

$$\mathcal{L}(\Theta) = \prod_{i=1}^m \frac{1}{\sqrt{2\pi\sigma^2}} \exp\left(-\frac{\Theta_i^2}{2\sigma^2}\right) \quad (11)$$

with free parameters μ and σ . These parameters do not affect the location of the maximum, so we do not define them. Given this likelihood, the log likelihood is proportional to $-\|\Theta\|^2$. Minimizing the norm of Θ is therefore equivalent to finding the maximum likelihood.

Putting aside the problem of minimizing the norm, we use the linearity of equations 2 and 1 to write $\mathbf{K} = M\Theta$, where the i th entry of every row of the $n \times m$ matrix M is the integral presented in equation 2 or 1, evaluated over the i th finite element. We want to solve $\mathbf{K} = M\Theta$ for Θ to match equation 8, which we do via the Moore-Penrose inverse. Since $m > n$, the Moore-Penrose inverse of M is

$$A = M^+ = M^*(MM^*)^{-1} \quad (12)$$

where M^* is the adjoint of M . The vector $\Theta = M^+\mathbf{K}$ is guaranteed to solve $\mathbf{K} = M\Theta$, and by the properties of the Moore-Penrose inverse, this Θ also happens to minimize the norm of all possible Θ that satisfy the equation. Thus, defining $A = M^+$ also minimizes \mathcal{L} and fully defines the model.

Note that this model is fast to compute; assuming fast matrix multiplication, the matrix inversion of equation 12 is fast because MM^* is an n -dimensional square matrix, which is very small compared to the number of finite elements m .

2.5.2 The “harmonic” model

We now explore a model that seeks to restrict the space of allowed density distributions a different way: we allow only the density distributions with zero Laplacian: $\nabla^2\rho = 0$ inside the asteroid (the harmonic distributions). We therefore call this model the “harmonic” model. The expansion of a harmonic function in spherical coordinates is given by

$$\rho(\mathbf{r}) = \sum_{\ell m} \Theta_{\ell m} \frac{R_{\ell m}^*(\mathbf{r})}{a_A^\ell} \quad (13)$$

where the terms which lead to $\rho \rightarrow \infty$ at the origin have been removed and $\Theta_{\ell m}$ are free (complex) parameters. Since ρ is real, we have $\Theta_{\ell m} = (-1)^m \Theta_{\ell, -m}$. By setting a maximum on ℓ , we restrict the number of degrees of freedom to $(\ell_{\max} + 1)^2$. Choosing the same maximum ℓ as the maximum ℓ for the $K_{\ell m}$ moments, we have $m = n - 1$ coefficients $\Theta_{\ell m}$ which can be stacked into an m -dimensional vector Θ .

Inserting equation 13 into equations 2 and 1, we get

$$K_{\ell' m'} = \sum_{\ell m} \frac{1}{\mu_A a_A^{\ell'} a_A^\ell} \Theta_{\ell m} \int_A d^3 r R_{\ell m}^*(\mathbf{r}) R_{\ell' m'}(\mathbf{r}). \quad (14)$$

This is an over-determined matrix equation $\mathbf{K} = M\Theta$, where M is an $n \times m$ matrix. The Moore-Penrose inverse can therefore be used again to find an inverse $A = M^+$ which yields approximately correct Θ (approximate in that the norm of the error vector between \mathbf{K} and $M\Theta$ is minimized). However, the form of the inverse changes due to the equation being overdetermined:

$$A = M^+ = (M^* M)^{-1} M^* \quad (15)$$

In the special case where the asteroid is a sphere of radius R , the matrix defined by equation 14 is diagonal, with entries

$$M_{\ell m; \ell' m'} = \frac{4\pi R^3}{\mu_A} \frac{R^{2\ell}}{a_A^{2\ell}} \frac{\delta_{\ell\ell'} \delta_{mm'}}{(4\ell^2 + 8\ell + 3)(\ell - m)!(\ell + m)!}. \quad (16)$$

A non-spherical perturbation will introduce small off-diagonal entries to M . This diagonal represents another interpretation of the physical meaning of $K_{\ell m}$; they are directly proportional through this form of M and the matrix equation $\mathbf{K} = M\Theta$ to the coefficients of the spherical harmonic expansion of the asteroid density in the case of a spherical asteroid.

2.5.3 The “lumpy” model

The above two simple models produce smooth density distributions that generally extend non-uniformity over large regions. In this section, we define a more complicated model which identifies discrete regions differing from the overall density of the asteroid to best fit the measured density moments. We call this model the “lumpy” model.

Suppose the asteroid contains N “lumps” of uniform mass μ_i displaced by distance \mathbf{x}_i from the asteroid centre of mass and superimposed on a constant-density overall asteroid shape which is known in the form of $\mathbb{1}(\mathbf{r})$. For simplicity,

	N		
	1	2	3
1	2	7	12
d	2	5	13
3	7	17	27

Table 1. Total degrees of freedom D as a function of N , the number of lumps modelled, and d , the number of independent axis lengths considered for each lump. The configurations with $D \leq$ the six known parameters not including K_{3m} are coloured black, and with $D \leq$ the 13 parameters including K_{3m} parameters are coloured gray.

we assume that all N regions are ellipsoids with d independent axis lengths. For example, $d = 3$ corresponds to an asymmetric ellipsoid, $d = 2$ corresponds to a symmetric ellipsoid, and $d = 1$ corresponds to a sphere. Recall that $\mathbb{1}(\mathbf{r})$ is known in the hybrid frame where the origin is the centre of mass of the asteroid. The displacement of the shape centroid from the centre of mass, which is the opposite of the net displacement of the discrete regions, is therefore observable from light curve analysis. The model therefore has $3(N - 1)$ positional degrees of freedom, along with N degrees of freedom for μ_i , Nd shape degrees of freedom, and 0, $2N$, or $3N$ rotational degrees of freedom for $d = 1, 2$, or 3 respectively. The sum of these degrees of freedom are displayed in table 1. These degrees of freedom should be compared to the known density moments and a_A , of which there are $(\ell_{\max} + 1)^2 + 1$. However, three of these are the centre of mass of the asteroid which is guaranteed to be correct, and one is the unconstrained total mass so the total number of known parameters is $(\ell_{\max} + 1)^2 - 3$, which is 13 when the second-order density moments are known and six when only K_{2m} are known. We assume that the degrees of freedom of this lumpy model are always fewer than the number of \mathbf{K} known, so that the model is overdetermined.

The net $K_{\ell m}$ components of such an ensemble obey

$$K_{\ell m} = K_{\ell m}^{i0} + \sum_{i=1}^N K_{\ell m}^{i1} \quad a_A^2 = a_0'^2 + \sum_{i=1}^N a_i'^2 \quad (17)$$

where $K_{\ell m}^i$ and a_i^2 obey the same definition as $K_{\ell m}$ in equation 2 and a_A in equation 1 respectively, but integrated over the i th lump. Crucially, note that we set normalizing factors $1/(\mu_A a_A^\ell)$ and $1/\mu_A$ in equations 2 and 1 equal to the values for the entire asteroid, not their counterparts for each lump. The zero-indexed parameters indicate the moments of the uniform-density asteroid medium surrounding the lumps. The prime in equation 17 denotes that the moments are calculated in the hybrid frame, with its origin at the asteroid centre of mass.

We can relate the primed moments to the moments calculated relative to each lump’s centre of mass via the translation rules for solid spherical harmonics:

$$K_{\ell m}^{i1} = \sum_{\ell' m'} (-1)^{\ell - \ell'} R_{\ell - \ell', m - m'}(\mathbf{x}_i) K_{\ell' m'}^i \quad (18)$$

$$a_i'^2 = a_i^2 + x_i^2 \frac{\mu_i}{\mu_A}$$

from Ref. van Gelderen (1998). The dummy indices ℓ', m' should only be summed over values in which $\ell - \ell' \geq 0$ and $|m - m'| \leq \ell - \ell'$. Here, μ_i is the added mass of lump i , while $K_{1m} = 0$ and K_{2m} incorporate the lump’s orientation

and moment of inertia ratios. Its volume is constrained by a_i^2 . These values map directly onto an ellipsoid shape via equations ??, so that if $K_{\ell m}^i$, a_i^2 , μ_i , and x_i are known, then the density distribution of the asteroid is known.

Note that if \mathbf{x}_i is known, then equation 18 are linear in $K_{\ell m}^i$ and a_i^2 . Therefore, if we define Θ to contain K_{2m}^i and a_i^2 for all i in some order, then equations 18 and 17 define a matrix equation $\mathbf{K} = \mathbf{C} + M\Theta$ which can be solved by setting A equal to the Moore-Penrose inverse of M (equation 15, since Θ is overdetermined). Note that the \mathbf{C} term of this equation came from the expansion of $K_{\ell m}^{i0}$ and a_0^2 , which is written in terms of the already-known displacement of the asteroid surface from its centre of mass and the already-known surface shape.

This model's strategy will be to choose \mathbf{x}_i and μ_i via a non-linear process, then fit for the values $K_{\ell m}^i$ and a_i^2 using the linear format described in section 2.4. The constraints on \mathbf{x}_i is

$$\sum_{i=1}^N \mathbf{x}_i \mu_i + \mu_0 \mathbf{x}_0 = 0 \quad (19)$$

where \mathbf{x}_0 is the known displacement of the centroid of the asteroid model from the centre of mass. There are also additional constraints, such as that \mathbf{x}_i should lie inside the asteroid which can be enforced manually. The overall mass of the asteroid is $\mu_A = \mu_0 + \sum_{i=1}^N \mu_i$, and has been set, so we may eliminate μ_0 from equation 19. The constraint is now a function of μ_i and \mathbf{x}_i for $i \geq 1$. The matrix equation defining M is overdetermined, but we would like it to have a solution nevertheless. We therefore solve for \mathbf{x}_i and μ_i to yield an M with close solutions. This is done by minimizing

$$|(M(\mathbf{x}_i, \mu_i)M^+(\mathbf{x}_i, \mu_i) - \mathbb{1})(\mathbf{K} - \mathbf{C})|^2. \quad (20)$$

which is the difference between \mathbf{K} resulting from the model and the true \mathbf{K} . Here, $\mathbb{1}$ is the identity matrix. Then $A = M^+$ defines the model. We cannot define $\mathbf{B}(\mathbf{r})$ such that $\rho(\mathbf{r})$ is linear in \mathbf{B} , but uncertainty on $K_{\ell m}^i$ can still be evaluated as Σ_Θ and these can be converted into uncertainties in the dimensions and orientations of the lumps. If the resulting density distribution is somehow excluded (it predicts negative density distributions, the lumps extend outside the asteroid, etc.), then another minimum of equation 20 can be used, or another combination of N and d listed in table 1.

3 RESULTS

3.1 Density moment extraction

To demonstrate the success of our fit process, we present example results of the MCMC fit described in section 2.3, applied to encounter data of the asymmetric reference asteroid. The fit results were consistent with the true density moments, and produced consistent data.

Figure 2 shows the spin data with uncertainty added. Data simulated given the best-fitting density moments (the mean of the PPDs) is overlaid in the top pane and the residuals are shown the bottom pane. Uncertainties are plotted on the residuals corresponding to the square root of the diagonal entries of the covariance matrix (correlations not included). The fit results are clearly consistent with the data.

Figure 3 shows a corner plot of the ten fitted PPD, marginalized to functions of one or two variables. The true parameters are shown as lines. Note that the true parameters usually lie within 1 or 2σ of the $\Delta K_{\ell m} = 0$, where $\Delta K_{\ell m}$ is the difference between the posterior $K_{\ell m}$ and the true $K_{\ell m}$. The PPDs are generally Gaussian and no degeneracy between fit components is visible. We performed 48 independent minimizations of the likelihood before the MCMC fit began, each with an initial point chosen randomly in the parameter space. All converged to the same minimum, further showing that the model lacks degeneracy.

3.2 Density distribution extraction

To demonstrate the success of our three density distribution extraction models, we show density distributions and uncertainties extracted for the asymmetric reference asteroid in figure 4. These distributions were made given the density moment PPDs extracted in the previous section, with a_A fixed. The surface is fixed as a triaxial ellipsoid with semi-axis lengths such that the true values of $K_{\ell m}$ are consistent with uniform density (equation ??).

Also in each pane of figure 4 is $\Delta K_{\ell m}$, the squared magnitude of difference between the fitted density moments and the density moments of the final distribution. This difference is non-zero due to numerical error in the likelihood model case, but for the harmonic and the lumpy models, they express the degree to which the extracted moments cannot be represented with harmonic or lumpy distributions respectively.

The likelihood and harmonic models produce mostly the same density distributions. This is generally true for uniform density asteroids, which have harmonic density distributions. Consequentially, $\Delta K_{\ell m}$ is low for the harmonic model. This similarity lends confidence that the models produced are truly representative of the asteroid since they are produced via two independent methods.

The distributions' non-uniformity is limited for the harmonic and likelihood models. This non-uniformity is driven by error in the estimates of the density moments. Note that most of the asteroid has density close to one in both cases, with densities of 40% or 160% of the mean attained only in small regions. The lumpy model yields a much more uniform distribution because it is designed to produce uniform lumps. However, it does not produce a density distribution consistent with those extracted from spin data (i.e., $\Delta K_{\ell m}$ is usually large). This is because the lump found extends outside the asteroid, violating the assumptions of the model — a sign that the lump found does not really exist inside the asteroid.

The size of uncertainty is such that the density distribution is consistent with uniform at most points for the harmonic and likelihood models (within $1-2\sigma$), with a small number of low-uncertainty regions that are less consistent with uniform. Uncertainty is generally larger towards the edges of the distribution, both for these shapes and for the shapes shown in the following sections.

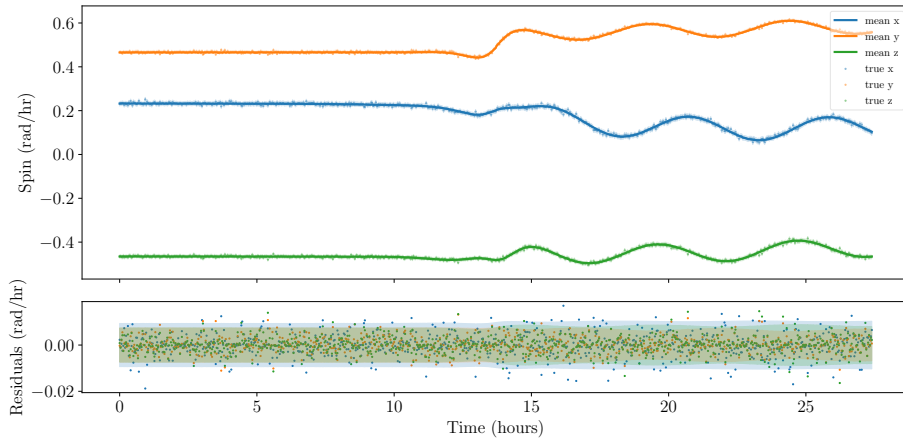


Figure 2. Data, best fit results, and residuals for a fit to synthetic data simulated for an asymmetric reference asteroid. The standard deviation of the data is plotted as an uncertainty band in the residuals plot, but these do not capture covariance between data points.

4 DISCUSSION

In this section, we discuss the physical properties of the asteroid encounter system (section 4.1), as well as the sensitivity of the density moment uncertainty to encounter properties (section 4.2), together with an analysis of advantages and disadvantages Jupiter encounters over Earth (section ??). Finally, we discuss the kinds of distributions produced by the density distribution extraction methods (section 4.4).

4.1 Spin evolution

In figure 5, we present example spin data generated via our simulation. A population of one thousand asteroids with identical initial conditions except for γ_0 , K_{20} , and K_{22} were simulated on a close Earth encounter. The exact parameters used were the symmetric and asymmetric cases described in appendix ???. Bands containing 68.3%, 95.5%, and 99.7% of the population’s spin are shown, as is the spin of the reference asteroids in black.

To choose the initial values of γ_0 , K_{20} , and K_{22} , spin data for the reference asteroids of appendix ?? was first generated. Then γ_0 , K_{20} , and K_{22} were re-extracted via the fit described in section 2.3. The population’s values for these parameters were PPD-distributed. However, the PPD distribution was widened by a factor of 1000 to make the band widths visible. Therefore, the scale of the bands in figure 5 have little meaning in an absolute sense, but they are meaningful when comparing two bands or two times in the same band.

The figure illustrates the sensitivity of spin data to asteroid density moments and γ_0 ; Before perigee, all asteroids had similar angular velocities, but after perigee the angular velocities of the population diverged. The oscillation periods observable during the torque-free precession phase of the spin data (about 5 hours after perigee) vary within the population, showing that they can be used to constrain K_{22} and K_{20} .

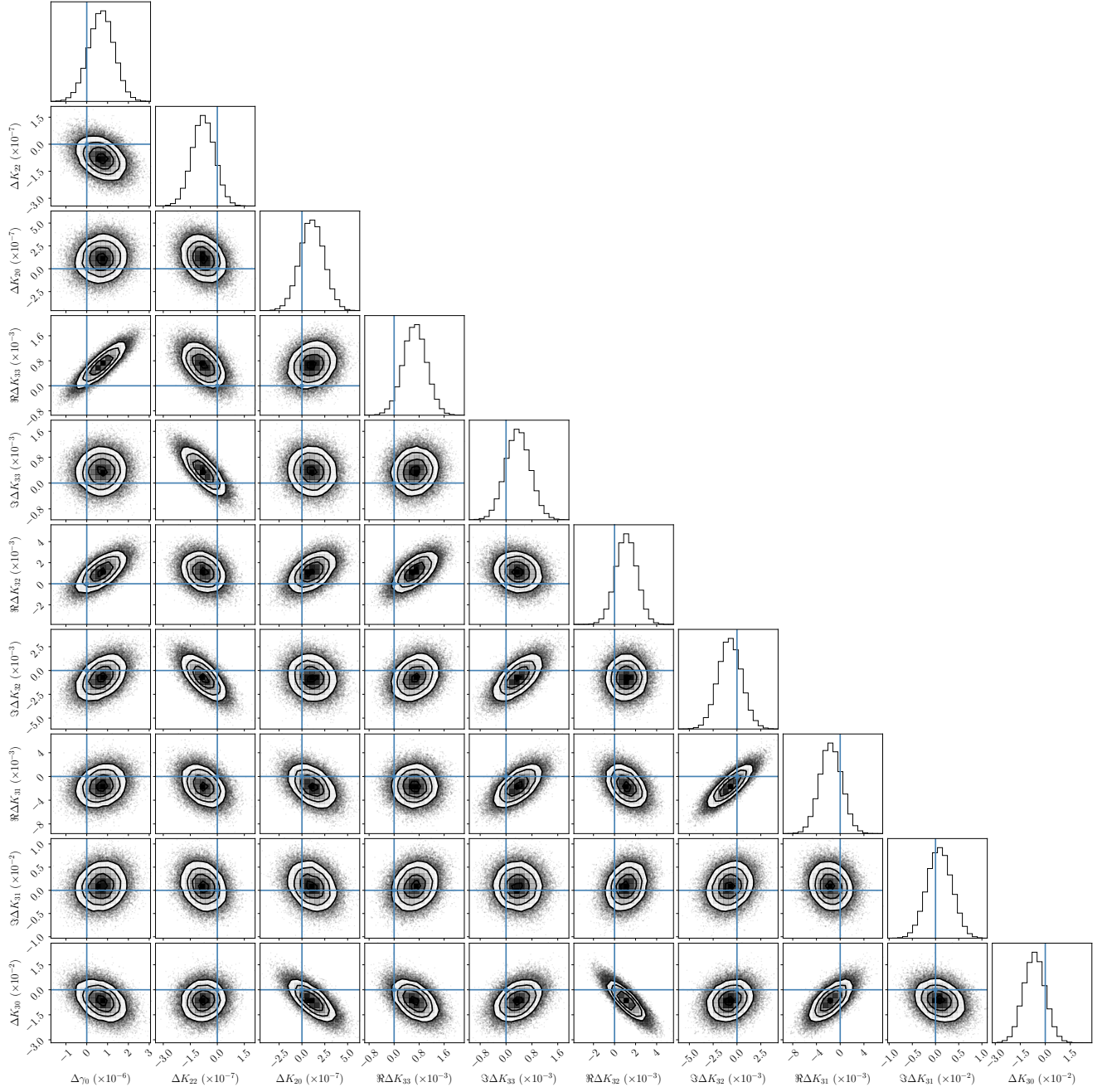


Figure 3. A corner plot for the fit results ten parameters to synthetic data simulated for an asymmetric reference asteroid. Marginal posterior PDFs for each parameter are shown (histograms) along with two-dimensional PDFs (contours). Individual points in the contours are samples from the MCMC fit, and the contours enclose 1, 2, and 3σ of them. True values (which are zero here due to the parameters being displayed relative to the true values) are also shown (blue lines).

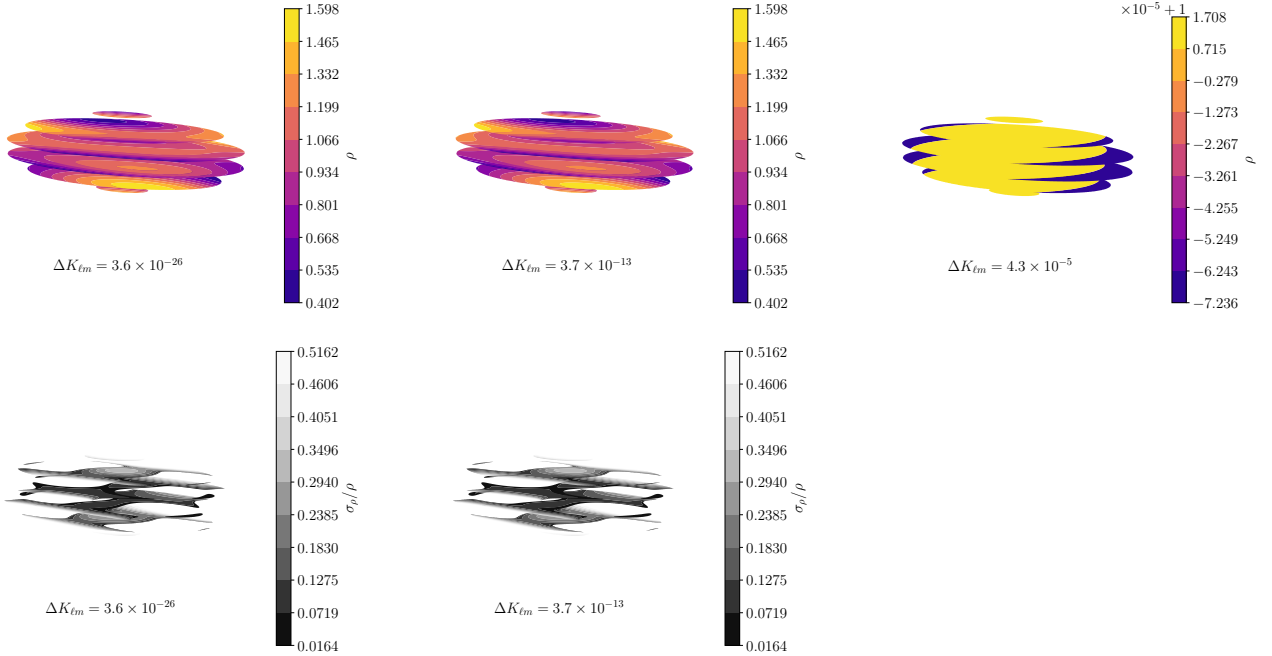


Figure 4. Density distributions (*top*) and uncertainties (*bottom*) extracted by the likelihood (*left*), harmonic (*middle*), and lumpy with $d = N = 1$ (*right*) models from data generated for a uniform-density, asymmetric reference asteroid. Density is normalized so that mean density is one.

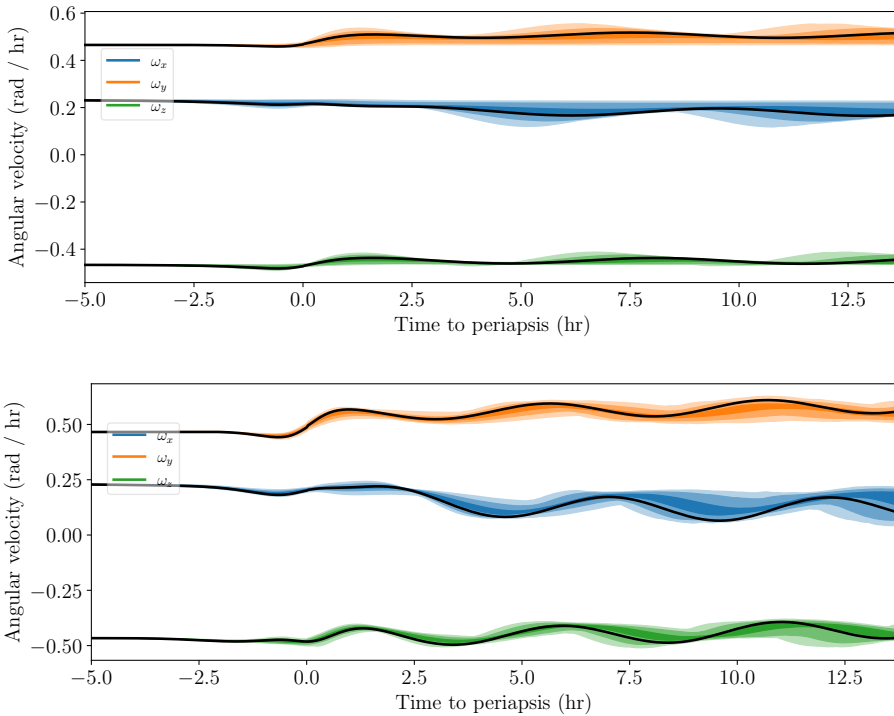


Figure 5. Angular velocity data simulated for the symmetric (above) and asymmetric (below) reference asteroids. The true angular velocity evolution is shown as a black line. Also plotted is the deviation of the data for PPD-distributed perturbations to the asteroid shape (bands). Bands contain 68.3%, 95.5%, and 99.7% of the 1000 simulations run.

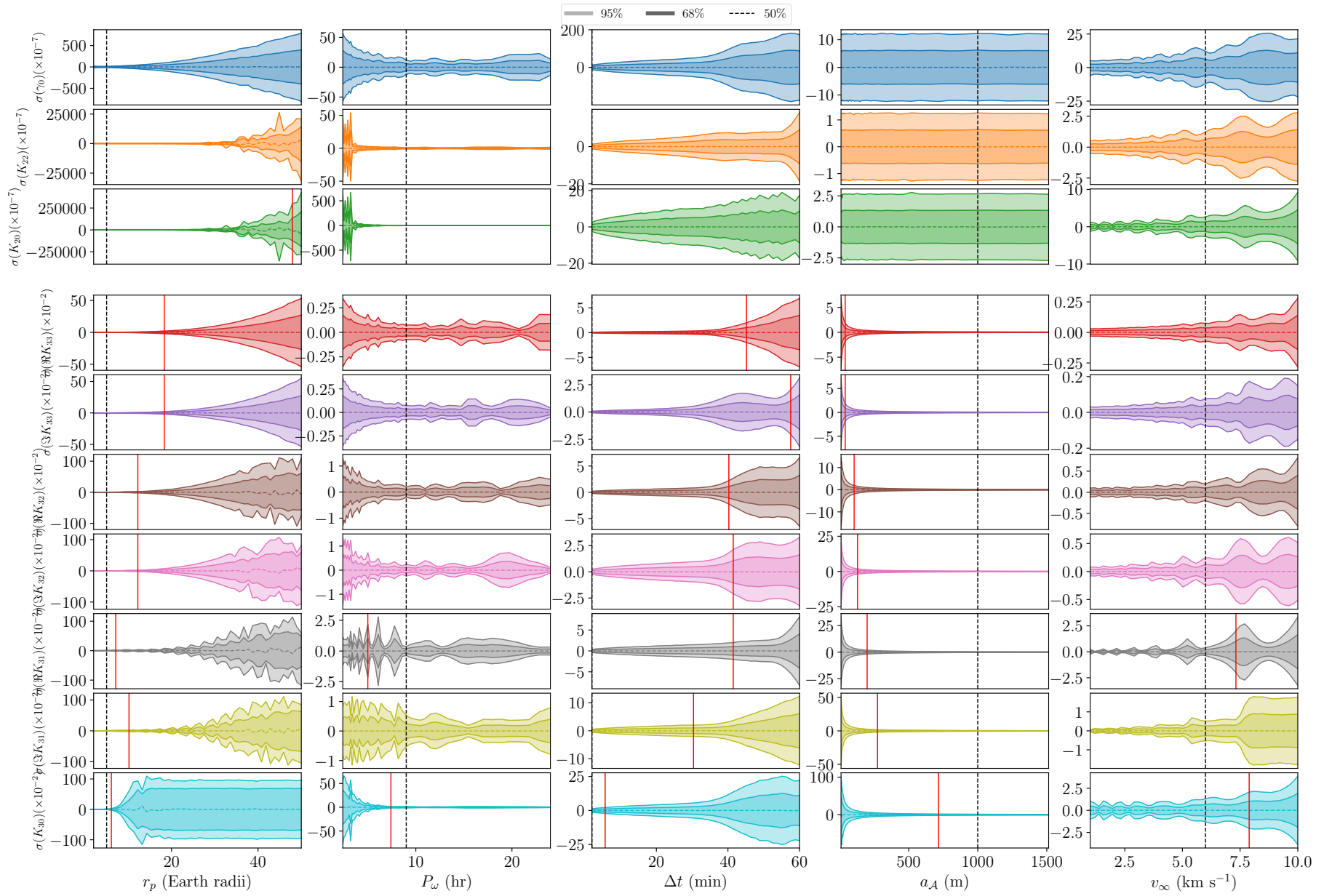


Figure 6. 1 and 2σ confidence intervals for the first-order parameter PPDs (*top*) and second-order parameters (*bottom*) as a function of various encounter parameters (*columns*). The vertical dashed line indicates the reference asteroid values of the parameters. The red vertical lines indicate when $\sigma = 0.01$.

4.2 Dependence of parameter uncertainty on encounter parameters

Parameter precision of 1σ is defined such that 68.27% of the PPD lies within 1σ of the mean of the PPD. 2σ is defined likewise for 95.45% of the PPD. The PPDs are usually roughly Gaussian, so that the upper and lower error bars are usually roughly equal and 1σ is approximately the standard deviation of the PPD. In all cases, we use the configuration of the asymmetric reference asteroid (appendix ??) unless otherwise stated.

4.2.1 Orbital elements

A Keplerian orbit is completely described by five parameters, but three describe the orbit's orientation with respect to the central body. The orbit can be rotated to the $\hat{\mathbf{X}}\hat{\mathbf{Y}}$ -plane, as mandated by our coordinate definitions, by changing the density moments of the central body. Since J_{00} is unchanged by this rotation and $J_{1m} = 0$, the orbit orientation is irrelevant until the J_{2m} terms of equation 3, and we do not investigate them here.

We parametrize the shape of the orbit by the perigee distance r_p and excess velocity v_∞ . Fits of the type described in section 2.3 were run for many values of r_p and v_∞ and the 1 and 2σ confidence intervals are displayed in figures 7 for v_∞ and ?? for r_p .

Figure 7 demonstrates that parameter precision does not depend strongly on excess velocity, aside from a slight trend especially in the higher order parameters for uncertainty to increase with v_∞ . This is likely due to the fact that larger v_∞ leads to a faster and flatter orbit with less time spent close to the planet, where tidal torque is strongest. There are also smaller-scale oscillations in the uncertainty, due to the orientation of the asteroid at perigee varying. The asteroid is always simulated to start at the same orientation, but increasing v_∞ decreases the time to perigee, so that the asteroid enters this region of high torque at different orientations depending on v_∞ . This effect explains why these small-scale oscillations have the same period for all parameters. Note that these oscillations are sometimes large enough to raise $\sigma > 0.01$, shown by the red vertical line.

Figure ?? shows much stronger dependence of parameter uncertainty on perigee distance, as expected by the factor of $(a_A/D)^{\ell'}$ present in equation 3 and mentioned in section ???. For $r_p \approx 6$ or 7 Earth radii, $\sigma(K_{30})$ reaches the reference 0.01 limit. At slightly higher r_p , K_{31} and K_{32} become similarly unresolved, and at $r_p \approx 20$ Earth radii, K_{33} , the last second-order component, becomes unresolved. Even before this, at $r_p \approx 10$ Earth radii, the most uncertain parameter K_{30} fills the prior distribution with uncertainty ranging from -1 to 1, visible by the sudden cut-off in uncertainty increase and the discontinuity of the σ curve there. The location of these limits will change if different encounter properties are used, but this is still an illustrative example.

Fitted to each of the curves in figure ?? are power law uncertainties $\sigma \propto r_p^\alpha$. These fits were performed via the method of least squares, and all data with $\sigma > 0.7$ was removed due to its sensitivity to the arbitrarily-chosen boundary of the prior. The values of α are shown in table 2. These slope values express how much each parameter is dependent on r_p . It is observed that γ_0 is least dependent on r_p , with

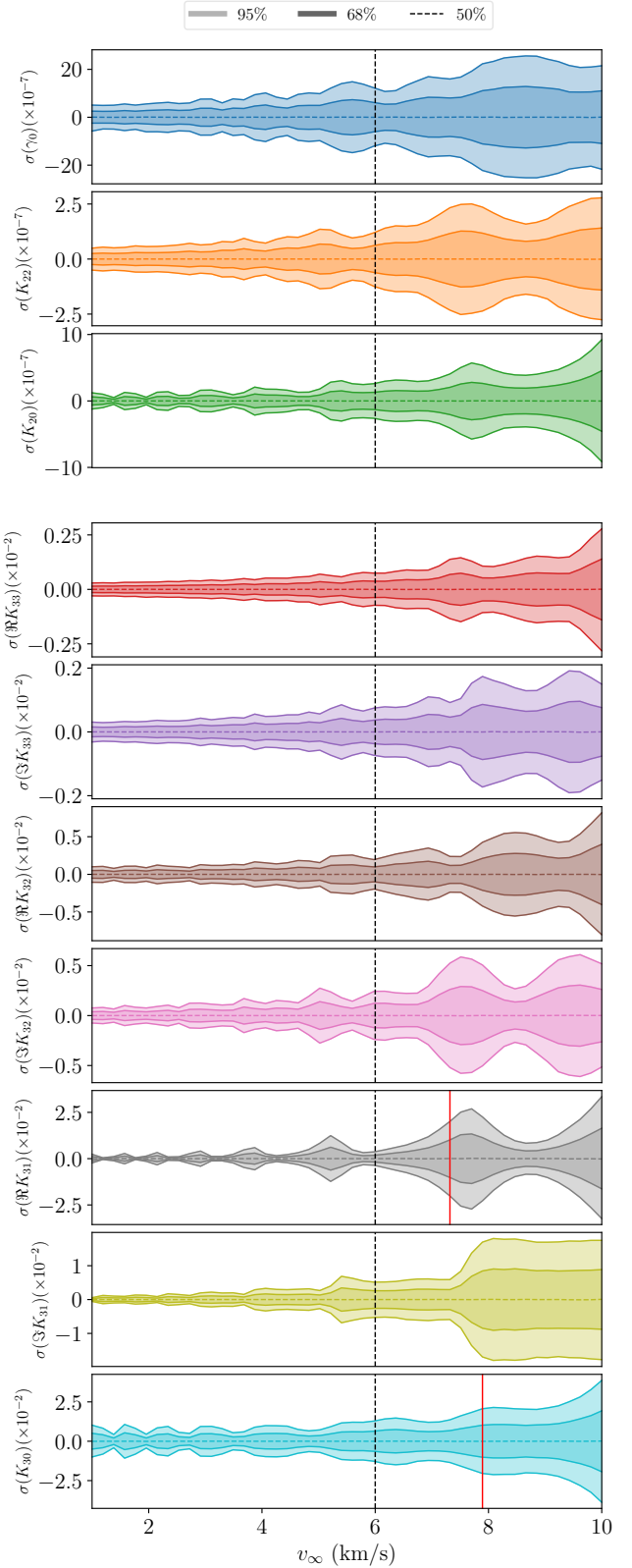


Figure 7. 1 and 2σ confidence intervals for the first-order parameter PPDs (top) and second-order parameters (bottom) as a function of orbital excess velocity v_∞ . The vertical dashed line indicates the reference asteroid value of 6 km s^{-1} . The red vertical lines indicate when $\sigma = 0.01$.

Parameter	α
γ_0	2.05
K_{22}	5.47
K_{20}	5.47
$\Re K_{33}$	3.35
$\Im K_{33}$	3.37
$\Re K_{32}$	3.05
$\Im K_{32}$	3.27
$\Re K_{31}$	3.53
$\Im K_{31}$	4.02
K_{30}	5.75

Table 2. Power law slope values for the dependence of parameter uncertainty on perigee distance r_p . Slope is defined by $\sigma \propto r_p^\alpha$.

$\sigma(\gamma_0) \sim r_p^2$. The other two first-order parameters are much more strongly dependent, with $\sigma \sim r_p^{5.5}$. The second-order parameters have milder slopes between 3 and 4 (except for K_{30}) which is fortunate from the perspective of making precise observations, since lower α renders larger values of r_p accessible to measuring K_{3m} .

The axes of figure ?? show that parameters with large m are more precisely determined than parameters with small m , as can be seen by comparing K_{22} to K_{20} and comparing K_{33} to other K_{3m} values. Large m moments correspond to moments that control higher frequency fluctuations in density at the asteroid equator. This pattern of large m corresponding to low uncertainty is a general trend and will be seen in the following sections as well.

The very strong dependence of σ on r_p makes this analysis only to extract second-order moments on close encounters. Fortunately, in the case of Earth, these encounters are also likely to have the best associated observational uncertainty when above the horizon due to their proximity. The first-order moments can still be extracted at much larger perigee distances in our model.

4.2.2 Observational Uncertainty

There are two parameters, σ_θ and σ_ρ , which govern the observational uncertainty of the data set (defined in section 2.2). Rather than explore the full space spanned by these two values, we measure how parameter uncertainties depend on the product of uncertainties $\sigma_\theta\sigma_\rho$ (with the radio fixed), and the ratio $\sigma_\rho/\sigma_\theta$ (with the product fixed).

We choose these metrics because we generally expect that the parameter uncertainty σ be proportional to the observational uncertainty, but whether the dependence is stronger on σ_θ or σ_ρ is not immediately clear. We get around this problem by varying σ_θ and σ_ρ together and fixing their ratio, and measuring the posterior uncertainty σ , with σ/σ_θ shown in figure ???. Indeed, we find that $\sigma \propto \sigma_\theta$ almost exactly, and since $\sigma_\rho/\sigma_\theta$ is fixed, we also have $\sigma \propto \sigma_\rho$. For large $\sigma_\theta\sigma_\rho$, the proportionality fails, but this is because $\sigma(K_{30}) \approx 1$ which fills the prior. Uncertainty cannot increase beyond this value.

We also investigate the dependence of posterior uncertainty on $\sigma_\rho/\sigma_\theta$ with $\sigma_\theta\sigma_\rho$ fixed in figure ???. If we simply had $\sigma \propto \sigma_\theta\sigma_\rho$, then σ would have no dependence on $\sigma_\rho/\sigma_\theta$. Any deviation from constant σ shown in the figure therefore reveals some additional dependence in the model on one of the observational uncertainties.

Indeed, figure ?? shows increased uncertainty when $\sigma_\rho/\sigma_\theta$ is large, so that σ depends more on σ_ρ than on σ_θ . We summarize this pattern by stating that, if the observer had to choose between better precision on the period or on the spin pole of the data, they should choose period. This is fortunate for observers since, **JTD: I want to say that precision on the period is better constrained by light curve analysis, but I do not know enough about light curve analysis to be sure.**

Another conclusion that can be drawn from figure ?? is that $\sigma(\sigma_\rho/\sigma_\theta)$ is proportional for all $K_{\ell m}$. The proportionality constant shows the same dependence on ℓ and m mentioned previously. The proportionality is broken near $\sigma \approx \pm 1$, where σ fills the prior.

The location of the $\sigma > 0.01$ limit demonstrates the great influence of observational precision on fit uncertainty; increasing $\sigma_\theta\sigma_\rho$ or $\sigma_\rho/\sigma_\theta$ by even a small amount raises $\sigma(K_{3m}) > 0.01$ in most cases.

4.2.3 Asteroid shape

The true values of $K_{\ell m}$, γ_0 , and a_A affect the uncertainties in extracted density moments σ . Here, we only investigate the sensitivity of σ to the first-order parameters and a_A . The K_{2m} moments can therefore also be viewed as the axes of a uniform density triaxial ellipsoid (equation ??).

In figure 8, we show the 1σ confidence intervals as a function of K_{20} and K_{22} , or alternatively a/c and b/c . We use axis ratios rather than the values of a , b , and c to remove the a_A dependence of equation ???. The figure shows large uncertainty in γ_0 for $K_{22} = 0$, or $a/c = b/c$, because K_{20} is rotationally symmetric around \hat{z} , and γ_0 is the initial orientation with respect to the \hat{z} axis. The data then have no physical dependence on γ_0 when $K_{22} = 0$. This induces degeneracy in the model which inflates uncertainties, not only in γ_0 but also the other components.

To remove the inflated uncertainty, one could assume a rotationally symmetric asteroid, remove γ_0 as a parameter, and run a fit. For a nearly rotationally symmetric asteroid however, a new parametrization is necessary which does not contain the ill-constrained γ_0 parameter. This task is beyond the scope of this paper, so we mostly consider asymmetric asteroids throughout.

Figure 8 also shows low uncertainty for highly asymmetric asteroids, where b/c and a/c are very different (i.e., when $|K_{22}|$ is large). Additionally, $\sigma(K_{20})$ and $\sigma(K_{22})$ decrease for large $|K_{20}|$, which corresponds to large axis ratios in the ellipsoid case.

Figure 9 displays the correlation between the first-order parameters for reference. They show that γ_0 and K_{22} are often correlated for asymmetric asteroids, while γ_0 and K_{20} are usually not. This is expected as K_{22} is dependent on the orientation of the asteroid and K_{20} is not. They also show that K_{22} and K_{20} are usually correlated, and that a/c and b/c are highly correlated. The latter is expected due to the $1/c$ dependence. As for the former, this correlation could likely be removed by an alternate parametrization, reducing uncertainties in the shape parameters.

Overall, the variation in the uncertainties on K_{20} and K_{22} (the first-order density moments) is present but largely smooth across their allowed parameter space, as is their correlation (except the large K_{22} corner). It therefore seems

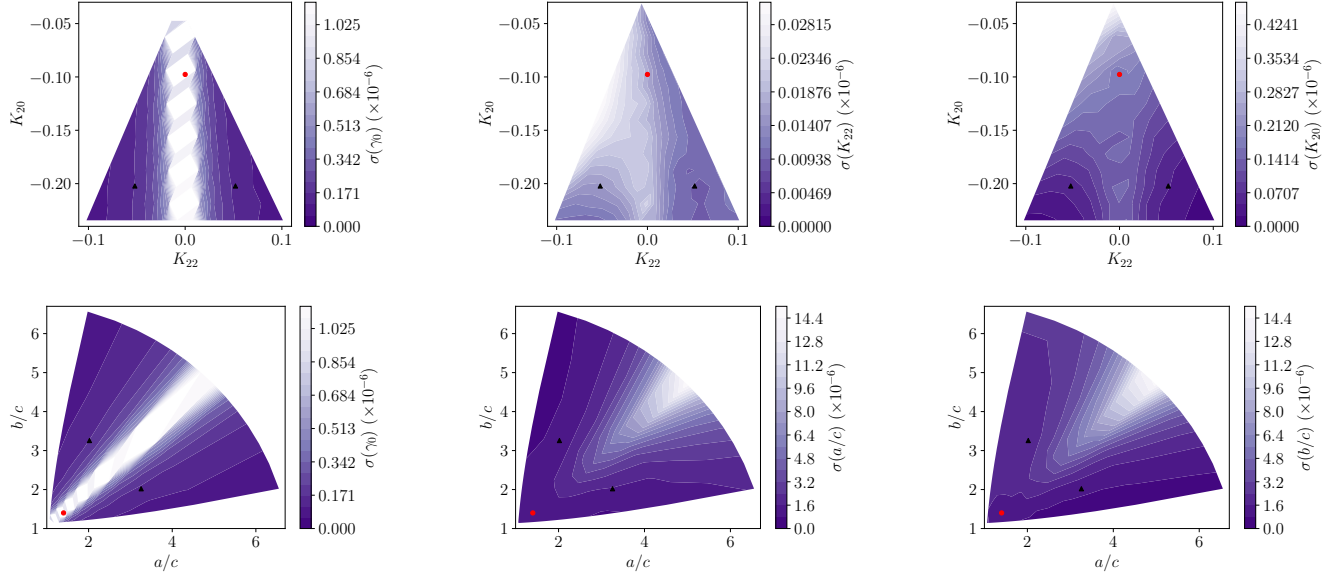


Figure 8. 1σ confidence interval for fit parameters γ_0 , K_{22} , and K_{20} (top row) and γ_0 , a/c , and b/c (bottom row). Also shown as black points are the reference asteroid shapes; the symmetric case is marked with a red circle and the asymmetric with a black triangle.

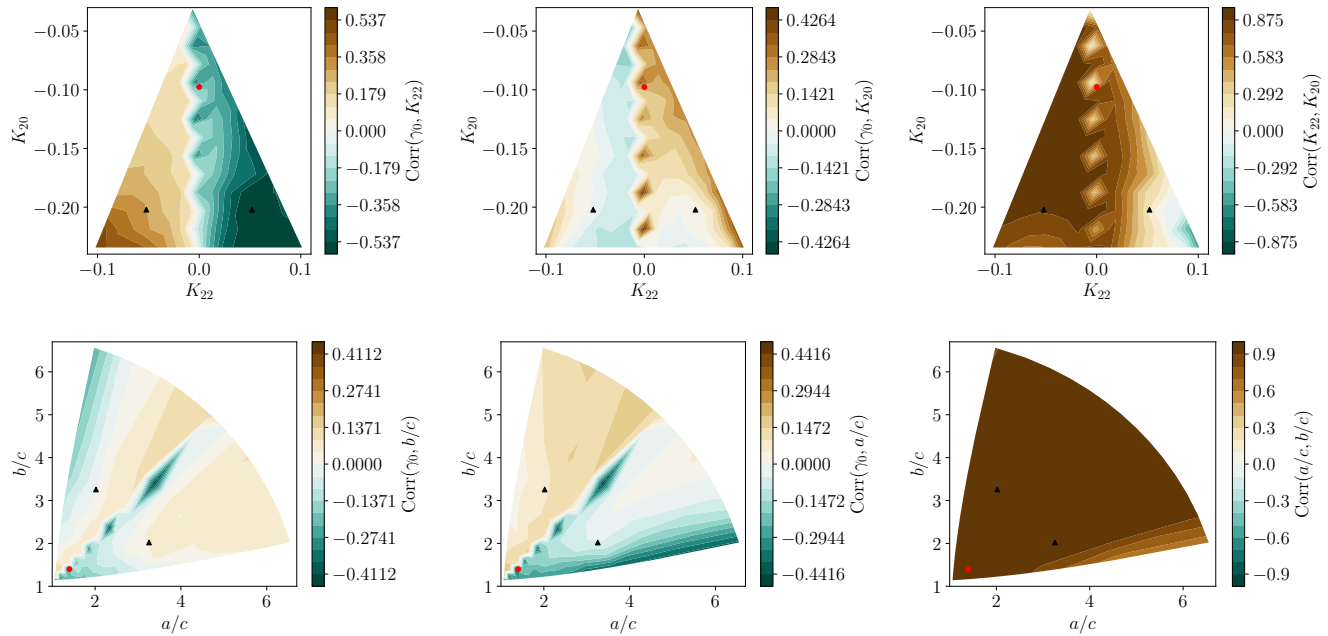


Figure 9. Correlations between PPDs for fit parameters γ_0 , K_{22} , and K_{20} (top row) and γ_0 , a/c , and b/c (bottom row). Also shown as black points are the reference asteroid shapes; the symmetric case is marked with a red circle and the asymmetric with a black triangle.

reasonable to use the asymmetric asteroid shape as a stand-in for an unknown's asteroid shape when simulating an encounter, as we do in this paper. The uncertainty then can be expected to differ across other shapes by a factor of about two or less, as long as the degenerate, symmetric asteroid regime is avoided.

On the other hand, the posterior uncertainty of K_{3m} is much more strongly dependent on asteroid length a_A . Figure 10 displays posterior uncertainty σ as a function of a_A , defined in equation 1. The vertical axis is shown in log

space, meaning that the average of the upper and lower error bars of σ is shown instead of showing both as is done in other figures.

As was mentioned in section ??, the K_{2m} parameters are insensitive to a_A since the a_A^2 term in τ (equation 3) is canceled by the a_A^2 in the moment of inertia (equation ??). The K_{3m} uncertainty is strongly dependent on a_A for the same reason that uncertainty is strongly dependent on r_p : the $(a_A/D)^{\ell'}$ dependence of equation 3. At $a_A \lesssim 700$ m, K_{30} becomes unresolved. The other parameters become

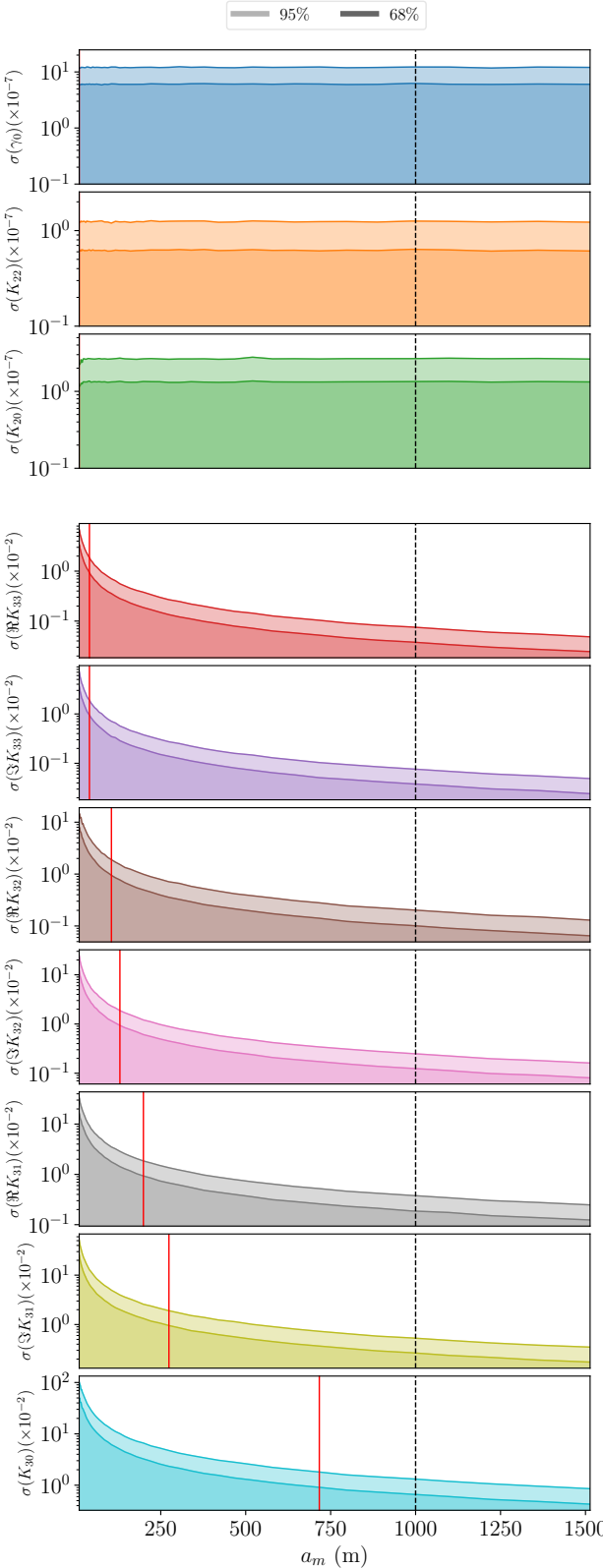


Figure 10. 1 and 2σ confidence intervals for the first-order parameter PPDs (*top*) and second-order parameters (*bottom*) as a function of asteroid length a_A . The reference cadence is 2 minutes. The red vertical lines indicate when $\sigma = 0.01$. The black dashed line indicates the reference value of $a_A = 1000$ m.

unresolved for $a_A \lesssim 300$ m, with the cut-off for K_{33} being less than 100 meters. This a_A cut-off is quite sharp; figure 10 shows steep decrease in $\sigma(a_A)$ for low a_A , with an approximate functional form of $\sigma(a_A) \sim e^{(a_A/C)^p}$ for a scaling constant C and some power $p < 1$. (In figure 10, the best fitting values are $p < 0.1$.) This sharpness indicates that the cut-off value of a_A is unlikely to change significantly if other parameters of the flyby are altered in a way that slightly increases or decreases σ . It therefore appears that extracting precise K_{30} from asteroids with $a_A \lesssim 700$ m is very unlikely with this analysis, and for $a_A \lesssim 50$ m, all K_{3m} will likely be unresolved.

For uniform density asteroids, large a_A is equivalent to large asteroid radius, which was mentioned in section ?? and explicitly shown in equation ???. In non-uniform density asteroids, large a_A can also be achieved by distributing the mass of the asteroid near the surface, because the r^2 term in the integrand of the definition of a_A causes the density of regions distant from the asteroid centre of mass to dominate a_A .

4.2.4 Cadence

The time between observations of asteroid angular velocity, or cadence, may vary depending on the observational schedule of the observing telescopes and the path of the asteroid through the sky. We measure how the posterior uncertainty σ varies with cadence ranging from two minutes to one hour in figure ??.

Figure ?? displays little dependence of uncertainty on cadence Δt for $\Delta t \lesssim 40$ min. We also see flaring of uncertainty for very large cadence, largely driven by the paucity of data points. However, uncertainty dramatically increases for many parameters at about $\Delta t = 30 - 40$ min, a time scale which is likely characteristic of the asteroid system. We name this rough cadence limit T_{cad} .

We expect T_{cad} to be a function of two dynamical time scales of the system: the rotational period of the asteroid P_ω and the time spent near perigee T_p . The latter can be estimated by

$$T_p \sim \frac{r_p}{v_\infty} \left[2 \frac{\mu_B}{r_p v_\infty^2} + 1 \right]^{-\frac{1}{2}} \quad (21)$$

which is the ratio of the perigee radius to velocity at perigee. The exact choice of the formula of T_p not obvious, and alternatives to equation 21 are possible. For the simulated asteroid, $P_\omega = 9$ hr and $T_p = 42$ min by this definition.

We further study the effect of P_ω and T_p on T_{cad} in appendix ??, and find that both affect T_{cad} by roughly the same amount.

Figure ?? shows that as long as $\Delta t < T_{\text{cad}}$ is achieved, the influence of cadence on σ is minimal (except for K_{30} where the $\sigma < 0.01$ limit is slightly exceeded). However, shorter cadence almost always leads to lower uncertainties.

4.2.5 Perigee gap

In certain circumstances, spin data might not be able to be captured for a close encounter at perigee. The asteroid might dip below the horizon, or it might pass too close to the sun to be observed. Generally, angular velocity data can

be collected when the asteroid is distant from the central body, where torque is low. There, the angular velocity evolution is dominated by torque-free precession dictated by the moment of inertia components. That zero-torque data can still be used to fix K_{20} and K_{22} as in Moskovitz et al. (2020). However, K_{3m} are not extractable from precession data alone. We are therefore curious as to how our posterior uncertainties change due to lack of data during the encounter perigee.

To test this, we mask the perigee of the counter by removing a duration T of data centred on the perigee, where T ranges from 0 to 3 hours. To prevent lack of precision on $K_{\ell m}$ induced by lower amounts of data for high T , we always cut 3 hr– T from the data set, half from the beginning and half from the end, so that each data set produced for all T has the same length of data before and after the perigee. We then fit the same asteroid model to the cut data for all T and plot posterior uncertainties σ in figure 11.

Since torque is greatest at perigee, we expect that region of the data to contain the most information about $K_{\ell m}$, and therefore uncertainty should increase monotonically with T , which is seen in figure 11. We also see that the first-order parameters are not as sensitive to T as the second-order parameters, because K_{2m} are additionally constrained by torque-free precession after perigee.

Most parameters show dramatically increased uncertainty in the $T \sim 1 - 2$ hr range. On the other hand, none of the uncertainties increase noticeably for $T < 30$ min. Thirty minutes of dropped data is equivalent to fifteen dropped points for the simulated cadence of $\Delta t = 2$ minutes, showing that many data points can be dropped from the data set at perigee before the uncertainty starts to increase.

Qualitatively, 11 shows similar dependence of σ on T as ?? showed for σ on cadence Δt . They also both have cut-offs where uncertainty markedly increases, and both the T and Δt cut-offs have qualitatively similar shapes although they occur at different values of Δt and T . This suggests that the factors that govern uncertainty due to cadence (appendix ??) also may govern sensitivity to lack of data at perigee in a similar way.

4.2.6 Initial spin pole

The tidal torque experienced by the asteroid is affected by the initial direction of asteroid spin Ω_0 both because spin sets the initial asteroid orientation up to γ_0 and because of the spin-dependence of the rotational equations of motion (equation ??).

In figure 12, we display 1σ uncertainties for all parameters as a function of the direction of Ω_0 , mapped onto the unit sphere in the inertial frame. Our samples for Ω_0 were laid out on a Fibonacci sphere to ensure they were roughly evenly spaced (marked in figure 13). To highlight common features across the parameters, we also display the average 1σ sensitivity in figure 13. The average is weighted such that the uncertainty map for each parameter contributes an equal amount (the weight of each map is set to one-tenth of the map's mean). This average map is presented in two different projections to allow data at \hat{Z} to be read.

Certain alignments of the body-fixed frame to the inertial frame lead to special conditions on torque, as discussed in section ???. For example, $z \parallel \hat{Z}$ and $z \parallel \hat{Y}$ at perigee lead

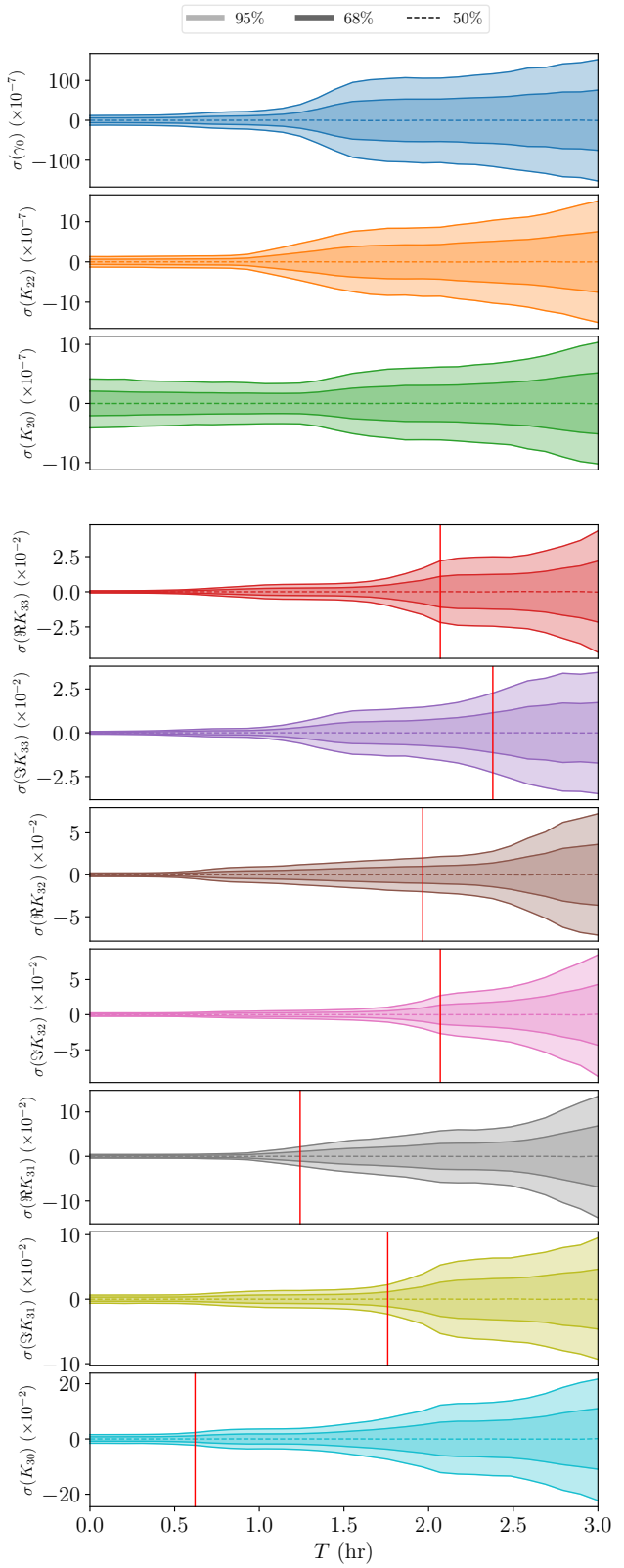


Figure 11. 1 and 2σ confidence intervals for the first-order parameter PPDs (*top*) and second-order parameters (*bottom*) as a function of a data gap of width T at perigee. The red vertical lines indicate when $\sigma = 0.01$.

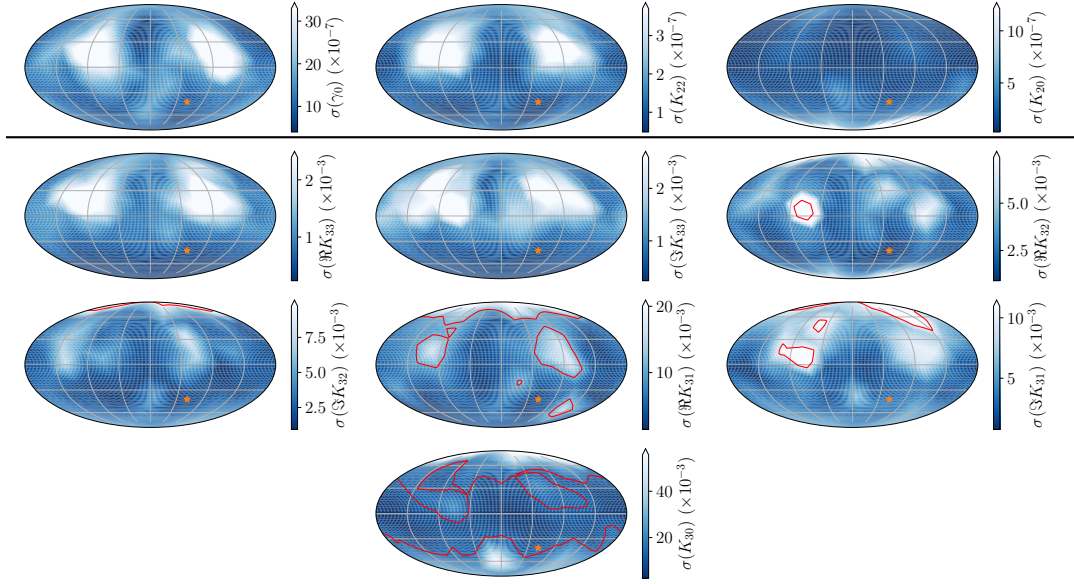


Figure 12. 1σ uncertainties for the first-order parameters (*top*) and second-order (*bottom*) as a function of the initial direction of spin in the inertial frame. All maps are made in the Mollweide projection. The orange star indicates the reference spin pole. The red contours enclose regions where $\sigma \geq 0.01$.

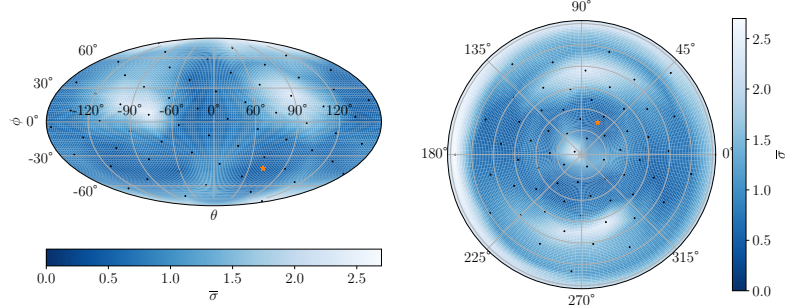


Figure 13. The weighted average of the uncertainties shown in figure 12, in Mollweide (*left*) and polar (*right*) projections in the inertial frame. See text for a description of how the average was computed. Black dots indicate the Fibonacci-sphere-distributed locations of sample spin poles, and the orange star indicates the reference spin pole. The polar projection is centred at the south pole, or $-\hat{\mathbf{Z}}$.

to $\boldsymbol{\tau} \parallel \hat{\mathbf{z}}$ to first-order, and $\boldsymbol{\tau} \parallel \hat{\mathbf{X}}$ at perigee leads to $\boldsymbol{\tau} = 0$ to first-order. We relate this to the initial direction of $\boldsymbol{\Omega}_0$, via the approximation that $\boldsymbol{\tau}$ is small until perigee. Then, since $\boldsymbol{\omega}_0 \parallel \hat{\mathbf{z}}$ in the body-fixed frame as an initial condition (section 2.1), we have that $\boldsymbol{\Omega}_0 \parallel \hat{\mathbf{Y}}$ and $\boldsymbol{\Omega}_0 \parallel \hat{\mathbf{Z}}$ both lead to $\boldsymbol{\tau} \parallel \hat{\mathbf{z}}$, and $\boldsymbol{\Omega}_0 \parallel \hat{\mathbf{X}}$ leads to $\boldsymbol{\tau} = 0$.

Figure 13 shows area of increased uncertainty for $\boldsymbol{\Omega}_0 \parallel \hat{\mathbf{Z}}$ and $\boldsymbol{\Omega}_0 \parallel \hat{\mathbf{Y}}$, but not the $\hat{\mathbf{X}}$ case. This indicates that $\boldsymbol{\tau} \parallel \hat{\mathbf{z}}$ causes increased uncertainty. Physically, $\boldsymbol{\tau} \parallel \hat{\mathbf{z}}$ only changes an asteroid's rotational period and does not cause it to tumble, eliminating the ability to discern moment of inertia ratios from zero-torque precession after the encounter. Also, τ_z affected by fewer parameters than τ_x or τ_y . Both of these are reasons why $\boldsymbol{\tau} \parallel \hat{\mathbf{z}}$ might inhibit precise fits to spin data. If $\boldsymbol{\tau} = 0$ to first-order, then second-order $\boldsymbol{\tau}$ and non-perigee $\boldsymbol{\tau}$ will dominate, which may increase precision to these usually non-dominant parameters and therefore not have the same increasing effect on σ .

It is important to note, however, that uncertainty does

not vary by much more than a factor of two outside the imprecise regions of $\boldsymbol{\Omega}_0 \parallel \hat{\mathbf{Z}}$ and $\boldsymbol{\Omega}_0 \parallel \hat{\mathbf{Y}}$, though these regions are wide for some parameters. Within the imprecise regions, uncertainty can grow up to four times or more the uncertainty at other $\boldsymbol{\Omega}_0$ values, and can exceed the $\sigma = 0.01$ benchmark. The trends for are roughly consistent across parameters (figure 12), leading to clearly visible imprecise regions in the average σ (figure 13).

4.2.7 Rotational period

We also study the effect of the initial rotational period of the asteroid P_ω on posterior uncertainty σ . The dynamical time scales r_p/v_∞ and $\mu_B/(r_p v_\infty)$ have already been mentioned in the context of the cadence cut-off (section 4.2.4), and the ratio between them and P_ω in principal may affect σ . In figure ??, we show σ as a function of P_ω for a range of periods typical of NEOs.

Like figure 7, depicting the dependence of σ on v_∞ ,

figure ?? shows small-scale variation in uncertainty due to the fact that varying the initial period changes the value of γ at perigee, which affects uncertainty to a factor of about two. But a large-scale trend is also visible in many parameters. K_{20} and K_{22} show very large uncertainty for $P_\omega \lesssim 4$ hr because these fast-rotators tumble very little after perigee. This increases uncertainty on the K_{2m} parameters, which are constrained by tumbling.

We expect that quickly rotating asteroids would not tumble because, for small P_ω , the dynamical variables D , ω , α , and β vary much smaller than γ . Approximating each variable as constant over one full rotation of γ , we can integrate the first-order contribution of τ over $\gamma \in (0, 2\pi)$ and reveal that each rotation has zero average first-order torque. Since the first-order torque over each rotational period cancels out, there is no secular torque to force the asteroid to tumble. However, this effect does not apply to the second-order parameters, since the integral over the second-order term of τ does not vanish, as seen in the figure.

Another feature of figure ?? is that $K_{\ell 0}$ is more uncertain at low P_ω than the other parameters. This is most visible in the figure for K_{30} . The cause is likely that $K_{\ell 0}$ cannot contribute to τ_z as shown in equation 3. We already discussed that asteroids with small P_ω do not tumble, and since τ_x and τ_y are what induces tumbling, the most observable component of torque is therefore τ_z , which $K_{\ell 0}$ do not affect.

The most severe effect of period on σ is in the low-period regime ($P_\omega \lesssim 5$ hr), but in this case, the most strongly affected parameters are K_{2m} , which are generally known better than K_{3m} . The effect on the imprecise parameters K_{3m} is small, except for K_{30} . It therefore seems as though small-period asteroids are still candidates for observation, although high-period asteroids still have better uncertainty.

4.2.8 Central body oblateness

In all the above studies, we assumed a spherical planet ($J_{\ell m} = 0$ for $\ell \geq 1$). By assumption that $\mu_B \gg \mu_A$ (so that the asteroid orbit's focus is the centre of mass of the central body), we have $J_{1m} = 0$. The effect of central body oblateness, then, is limited to the J_{2m} terms, and therefore damped by a factor of $(a_B/D)^2$. We expect these parameters to have little effect on the asteroid.

Here, we define oblateness as $\epsilon = (I_z - I_x)/(\mu_B R_M^2)$, where $I_{x,y,z}$ are the central body moments of inertia along the principal axes, and $I_x = I_y$. R_M is the true radius of the body (not a_B from equation ??).

$J_{\ell m}$ is defined in equation ?? with respect to the asteroid orbit, not the principal axes of the central body. However, for an equatorial orbit, the central body principal axes coincide with the asteroid orbit frame and we may express ϵ simply in terms of $J_{\ell m}$ as $\epsilon = -2J_{20}$ and $J_{22} = 0$. (Some sources such as Ref. Pater & Lissauer (2015) take $\epsilon = J_{20}$ as their definition of J_{20}). For simplicity, we use this equatorial orbit case. If the orbit is non-equatorial, the other J_{2m} terms will be non-zero. Since an oblate ellipsoid is mirror-symmetric around all three axes, table ?? indicates that J_{3m} are all zero. The next order of precision after this oblateness approximation is therefore J_{4m} , damped by an additional $(a_B/D)^2$ factor, and non-ellipsoid corrections to the central body shape.

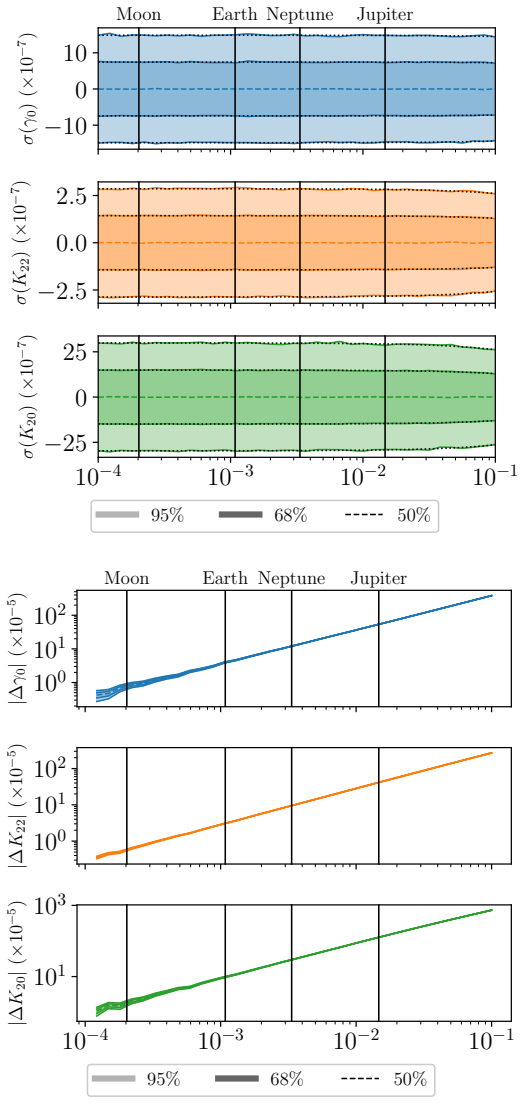


Figure 14. Top: 1 and 2σ confidence intervals for the first-order parameter PPDs as a function of oblateness ϵ . Linear best-fitting lines to σ (black, dotted) are plotted. Bottom: The difference between PPD means extracted from a zero-oblateness model and the true parameters given data with true oblateness $\epsilon_{\text{true}} \neq 0$. Also shown in both figures are the oblatenesses of reference Solar System bodies.

Given this conversion between ϵ and J_{20} , we analyze posterior uncertainty σ of the first-order parameters as a function of ϵ across a reasonable range of central body oblatenesses based on those of Solar System planets Pater & Lissauer (2015). These uncertainties are shown in the top pane of figure 14, together with linear best-fitting curves for $\sigma(\epsilon)$.

The figure demonstrates a small dependence of σ on oblateness ϵ , but the effect is far from important compared to the other factors studied above. Most Solar System bodies do not reach the oblateness necessary to significantly increase precision on the first-order parameters. The best-fitting lines match the uncertainties well, and they have slope of $(\Delta\sigma/\sigma_{\epsilon=0})/\Delta\epsilon = -0.26$ for γ_0 , -0.94 for K_{22} , and -1.2 for K_{20} . The second-order parameters K_{3m} likely de-

pend on oblateness similarly, but fitting these parameters is computationally more expensive and we do not study them here.

Note that if an encounter is executed around one of the non-Earth objects noted in figure 14, a_B and μ_B will change in addition to ϵ . These two parameters also affect the precision of the fit parameters (appendix 4.3), so the figure does not show that encounters with other bodies have the same precision as encounters with Earth; only that the difference in oblateness between the two bodies is of little concern.

Given the small effect of ϵ on $K_{\ell m}$, it might be tempting to neglect the planetary oblateness when fitting $K_{\ell m}$ to data. However, the bottom pane of figure 14 demonstrates that doing so is invalid. This figure displays $K_{\ell m}$ as extracted by a fit assuming $\epsilon = 0$, but run on data generated with non-zero ϵ . The difference between the PPD means and true parameters are shown. Posterior uncertainties are also shown as bands. The figure shows that even for low (Moon-scale) oblateness, the fit results are inconsistent with the true $K_{\ell m}$ values, since $\Delta K_{\ell m} = 0$ is not contained in the 2σ band. This effect is much worse for large oblateness, growing to a difference on the order of 10^{-2} between the true and fit parameters for large oblateness. Therefore, accurately modelling central-body oblateness to high precision is essential for accurate estimation of fit parameters. For non-equatorial orbits, with $J_{22} \neq 0$, we also expect J_{22} to affect the accuracy of the fit results to a similar degree, with the additional requirement of using the correct asteroid orbital plane.

Note that J_{20} , the parameter studied in this section, has a slightly more general definition than oblateness. If the planet has a moon, the integral defining J_{20} (equation ??) can be extended to include this extra mass. Since J_{20} is a second moment, this effect is magnified for large distances of the mass from the central body centre of mass (though the effect is not quite quadratic because a_B also increases for large distances, and J_{20} is divided by a_B^2). This process is only valid when the asteroid never passes inside the moon's orbit.

As an order-of-magnitude estimate for this effect, two spherical objects with masses and radii of Earth and the Moon, separated by one Lunar distance, and both lying in the orbital plane has a combined $J_{20} = 0.25$. Extrapolating posterior uncertainty by the slopes of the best fit lines given earlier, this represents a decrease in $\sigma(K_{2m})$ by a factor of about one quarter.

This analysis suggests that large moons such as ours can improve fit quality, but further study of this effect is beyond the scope of this paper. Without a moon to inflate the oblateness of the central body, planetary oblateness does not significantly improve posterior uncertainty. However, correct representation of oblateness is essential to accurately estimate $K_{\ell m}$.

4.3 Comparison of Jupiter and Earth encounters

If sufficiently accurate spin pole data can be detected for non-Earth encounters, it may be possible to extract density moments for encounters with larger planets. In this appendix, we run our reference asteroid through a Jupiter encounter to analyze the differences in uncertainty.

The physical parameters of the asteroid body are kept

$K_{\ell m}$	$\sigma_{\text{Jupiter}}/\sigma_{\text{Earth}}$
γ_0	1.6
K_{22}	2.3
K_{20}	11
$\Re K_{33}$	18
$\Im K_{33}$	18
$\Re K_{32}$	18
$\Im K_{32}$	18
$\Re K_{31}$	25
$\Im K_{31}$	10
K_{30}	53

Table 3. Ratio of posterior uncertainty for all density moments $K_{\ell m}$ between an Earth encounter and a Jupiter encounter with identical properties except for an increased perigee.

the same as the Earth encounter case (listed in appendix ??), as are the observational uncertainty and cadence. The orbit is adjusted for the Jupiter case by setting a perijove distance of $r_p = 5$ Jupiter radii (compared to perigee radius $r_p = 5$ Earth radii for the Earth encounter). We perform two fits, each with a different value of v_∞ : in one case we keep the Earth-encounter value of $v_\infty = 6 \text{ km s}^{-1}$, and in the other case we increase the velocity such that the eccentricity (and therefore the angle between the orbits' hyperbolic asymptotes) are the same for both encounters. The latter requires $v_\infty = \sqrt{G\mu_B/r_p(e-1)} = 32 \text{ km s}^{-1}$. The rationale for these excess velocity values is that, for $v_\infty = 6 \text{ km s}^{-1}$, we keep a physically typical encounter excess velocity at the expense of changing the orbit shape, whereas for $v_\infty = 32 \text{ km s}^{-1}$ the orbit shape is unchanged, although the asteroid speed is dramatically increased.

Section 4.2.1 found that v_∞ does not affect the posterior uncertainties, and indeed we find very little difference between the two v_∞ cases. We therefore do not distinguish between the two cases further. The ratio between the posterior uncertainties in the Jupiter and the Earth encounters are shown in table 3. In all cases, the Jupiter posteriors are more uncertain than Earth posteriors.

These uncertainty ratios can be understood as follows. The leading order of tidal torque is proportional to μ_A/D^3 . If D/a_B (the ratio of the encounter distance to the central body radius) is roughly constant (as in this case, where $r_p/a_B = 5$), then $\mu_A/D^3 \propto \rho_B$ where ρ_B is the density of the central body. Therefore, little advantage is to be gained by looking for encounters of a massive planet in this sense. Since Jupiter is less dense than Earth, we expect that uncertainty in the first-order parameters γ_0 and K_{2m} would be slightly worse than in the case of Earth, which is seen in table 3.

The second-order terms are damped by an additional factor of a_A/D , which decreases if a massive central body is used. Since Jupiter is about 10 times larger in radius than Earth, we expect that the K_{3m} terms are about ten times more uncertain than the K_{2m} components, which is the case.

The $K_{\ell 0}$ components differ in that $\sigma_{\text{Jupiter}}/\sigma_{\text{Earth}}$ is about five times greater for $K_{\ell 0}$ than other moments of the same ℓ . In fact, K_{30} essentially fills the prior. The special properties of $K_{\ell 0}$ have been analysed noted before, in that they are always more uncertain than other moments and are particularly uncertain in regimes where the asteroid does not tumble after the perigee. In this case, the Jupiter encounter resulted in less tumbling than the Earth encounter, so the

larger increase in uncertainty in $K_{\ell 0}$ shown in table 3 is expected.

There are additional effects of central body mass which are not captured in this analysis. For example, encounters with massive planets are more plentiful, so that observation for a fixed period of time will lead to a larger number of observed encounters conducive to low-uncertainty moment extraction (large a_A , small r_p , etc.). The distribution of r_p in this encounter sample will also change; the ratio of the orbit impact parameter (the distance between the orbit asymptotes and the central body) to perigee distance is

$$\frac{b}{r_p} = \sqrt{1 + 2 \frac{G\mu_B}{r_p v_\infty^2}}. \quad (22)$$

It was mentioned above that the observable perigee distance r_p increases with $a_B \sim \mu_B^{1/3}$, so that $\frac{b}{r_p}$ is larger for more massive planets and therefore the same impact parameter leads to lower periapse. Other effects, such as a change in the physical properties of the encountering asteroids, may also affect the fit uncertainties.

Table 3 shows that an encounter with Jupiter yields less precise posteriors than an encounter with Earth, all else being equal. However, these selection biases will cause more large- a_A and small- r_p asteroids to encounter Jupiter, and therefore yield increased precision. Which of these contradicting effects dominates is not immediately clear, and depends on the specific asteroid population near Jupiter.

4.4 Comparisons between density models

To test the properties of the three density models defined in section 2.5, we simulate several asteroids with different shapes and density distributions on a close Earth encounter with the reference asteroid orbital and observational parameters. Density moments are extracted via our fit process and density distributions extracted by the three above methods. Below, we compare the resulting distributions to understand the performance of the extraction methods.

4.4.1 Uniform density test asteroids

We simulate several asteroids with uniform density distributions and ask whether a uniform distribution is recovered. This was already done in section 3.2 for the asymmetric reference asteroid. Here, we perform the same process for the symmetric reference asteroid, a ‘‘dumbbell’’ (two spheres of equal radius conjoined such that the surface of one intersects the centre of the other), and a tetrahedron. We use these shapes as rough approximations of potential shape types (i.e., a contact binary for the dumbbell, a polyhedron for the tetrahedron), but also to demonstrate the density models’ efficacy on sharp corners. The extracted distributions for all three models are shown in figure 15.

From figure 15, it can be seen that the likelihood and harmonic models produce mostly the same density distributions. This is generally true for uniform density asteroids, which have harmonic density distributions. Consequentially, $\Delta K_{\ell m}$ is low for the harmonic model. This similarity lends confidence that the models produced are truly representative of the asteroid since they are produced via two independent methods.

The dumbbell asteroid, like the asymmetric asteroid of figure 4, produces distributions whose non-uniformity is limited to a factor of 2 or less for the harmonic and likelihood models. This non-uniformity is driven by error in the estimates of the density moments. Note that most of the asteroid has density close to one in both cases, with the factor of two reached only by small regions. The lumpy model yields a much more uniform distribution, because it is designed to produce uniform lumps. Note that its uncertainty $\Delta K_{\ell m}$ is usually large, both because the model is severely overdetermined (it has 2 degrees of freedom) and because the lump found extends outside the asteroid, violating the assumptions of the model. This is a sign that the lump found does not really exist inside the asteroid.

The symmetric and tetrahedral asteroids are less-well represented by the density distribution model results. In both cases, the likelihood and harmonic models produce sometimes-negative distributions, and non-uniformity is especially large in the tetrahedral case. This is not the fault of the density models, but rather because both of these asteroids have $K_{22} = 0$ and (as discussed in section 4.2.3), this leads to degeneracy in γ_0 and inflated uncertainty in the density moments. In the tetrahedral case, the problem is worsened because $K_{20} = 0$ as well, so that torque is dominated by the small and ill-constrained K_{3m} components.

Uncertainty in each distribution was calculated but not shown. The size of uncertainty is such that the density distribution is consistent with uniform at most points for all models (within $1-2\sigma$), with a small number of low-uncertainty regions that are less consistent with uniform. Uncertainty is generally larger towards the edges of the distribution, both for these shapes and for the shapes shown in the following sections.

From these examples, we may draw the conclusions that all three models produce density distributions generally consistent with uniform for uniform asteroids. The most likely distributions (i.e., the ones shown in the figures) are themselves mostly uniform, but can still produce non-uniformities as large as a factor of 2 in certain regions due to uncertainty in $K_{\ell m}$. Asymmetric asteroids such as the dumbbell and the asymmetric reference asteroids yield the best results because they have $K_{22} \neq 0$ and therefore do not suffer from degeneracy in initial orientation. Finally, the lumpy model can generally be ruled out in these cases because it produces unphysical results.

If desired, the parameters of the models can be reduced to only fit the K_{2m} density moments; this will produce exactly uniform distributions, since it is equivalent to assuming $K_{3m} = 0$. However, doing so ignores the observational insight we gain from our fits to K_{3m} , so it is only valid when K_{3m} are too poorly constrained to be used.

4.4.2 Spherical shape test

We test the sensitivity of the density distributions to incorrect estimates for the shape of the asteroid by obtaining density moments from an ellipsoidal asteroid encounter and extracting density distributions assuming a spherical shape. We do this for the asymmetric and symmetric reference asteroids, with density distributions shown in figure 16.

Both the likelihood and harmonic models are accurate in that $\Delta K_{\ell m}$ is low, and they produce similar distributions

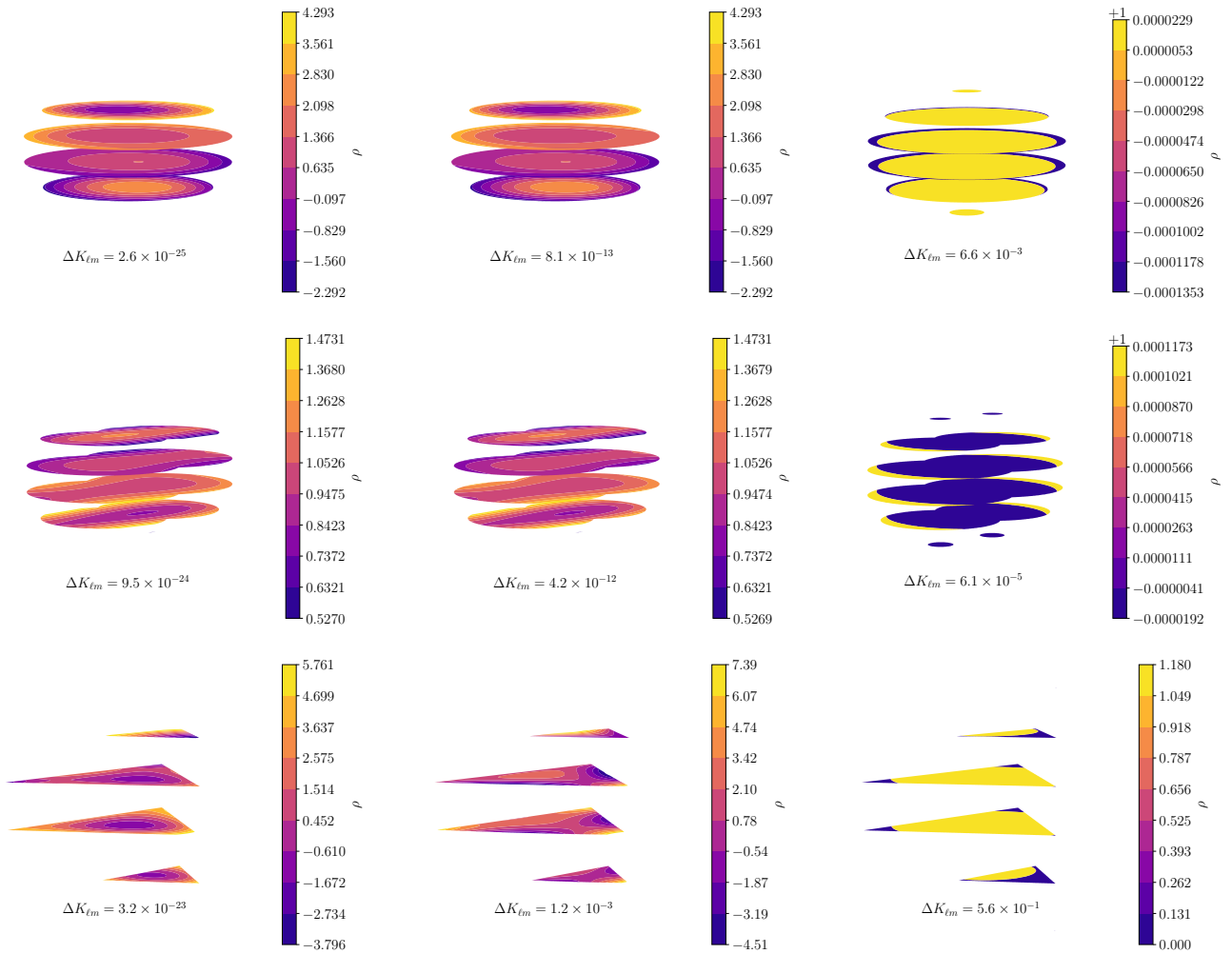


Figure 15. Density distributions extracted by the likelihood (*left*), harmonic (*middle*), and lumpy with $d = N = 1$ (*right*) models from data generated for a uniform-density asteroid. The asteroid shapes are, from top to bottom, the reference symmetric asteroid, the dumbbell model, and a tetrahedron. Density is normalized so that mean density is one. The same distance scale is used in all figures.

as in the previous section. However, now they both produce negative density distributions for both asteroid shapes. (In the previous section, only the symmetric model did.) This is a signal that the shape model is incorrect, and indeed the density distribution allows us to determine exactly how the shape model is wrong. In the asymmetric ellipsoid case, the density distribution is small (even negative) at large $|z|$ (top and bottom of the figure). The density is large at large $|y|$ (front right and back left in the figure). Comparison with the asymmetric reference asteroid depicted in figure 15 shows that the low-density region is outside the true asteroid shape, and the high-density region is inside. In other words, the shape can be corrected by extending it where density is large and retracting it where density is low.

A similar statement is true for the symmetric ellipsoid case in that density is low near the poles, but this time the regions with large density are evenly distributed around the equator, indicating the symmetry of the original asteroid.

The lumpy model produces lumps so large that they dominate the asteroid, predicting uniform distribution with $K_{\ell m} = 0$ for $\ell \geq 1$. The error in density moments $\Delta K_{\ell m}$

is therefore very large, equal to the sum of $|K_{\ell m}|$ for the original asteroid, making it clearly a poor model.

In short, severely incorrect shape estimates can be caught for all three models by negative predicted densities or by the failure of the density distribution model to match the extracted density moments. The shape can be corrected by extending it where the density distribution is high and retracting it where the density distribution is low.

4.4.3 Nonuniformity test

We also test several non-uniform density asteroids and compare the generated density distributions for all three models to see if the non-uniformities are recovered. We consider two asteroids, one with mass concentrated in the middle, and one with mass concentrated around the edges. (Specifically, the mass distribution follows a spherically symmetric exponential $\rho(r) \propto e^{\pm r^2/a_A^2}$). To prevent the problems seen in previous sections when a symmetric asteroid is simulated, we set the shape of the asteroids to the asymmetric refer-

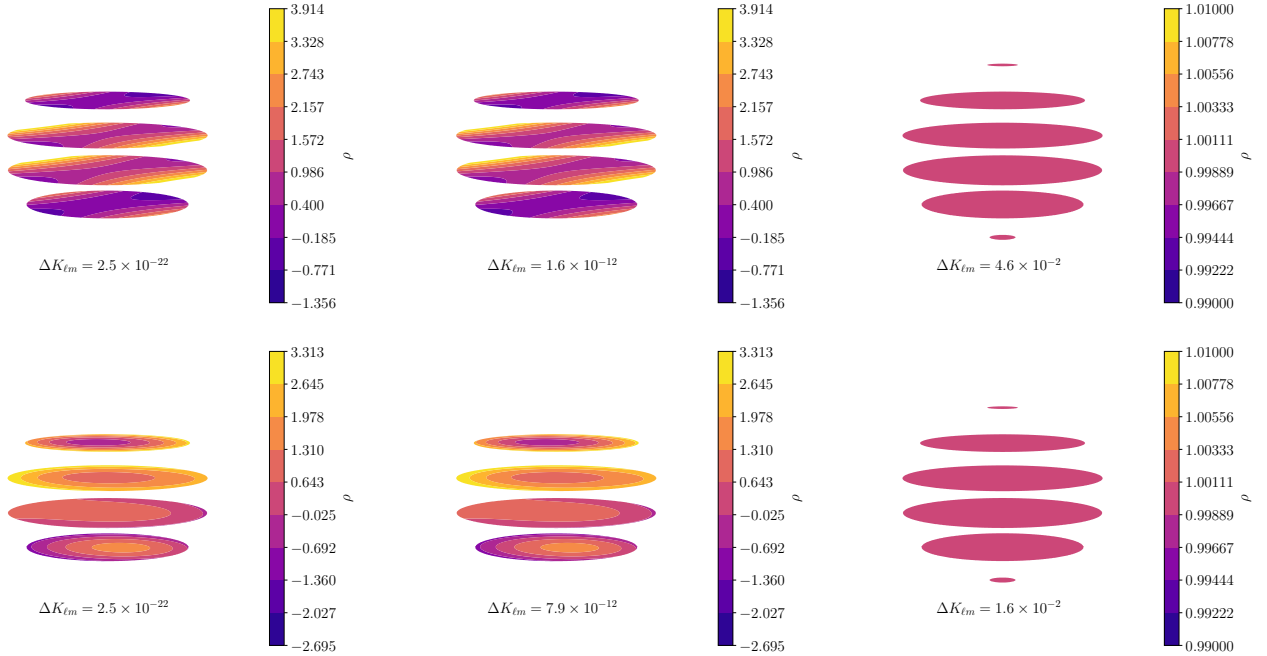


Figure 16. Density distributions extracted by the likelihood (left), harmonic (middle), and lumpy with $d = N = 1$ (right) models from data generated for a uniform-density asteroid. The original asteroid shapes were the reference asymmetric (top) and symmetric (bottom) ellipsoids. In both cases, the density distributions have been extracted assuming a spherical shape. Density is normalized so that mean density is one. The same distance scale is used in all figures.

ence asteroid. The extracted density distributions are shown in figure 17

For these non-uniform asteroids, the likelihood and harmonic model do not coincide, as can be seen by comparing the density distributions and the fact that ΔK_{lm} is much larger for the harmonic distribution (indicating that the true density distribution is not harmonic). However, the two models do give similar results. Comparing the centre-weighted asteroid and the edge-weighted asteroid distributions, one can see that the centre-weighted case indeed places more mass in the centre of the asteroid shape for the harmonic and likelihood models, while the edge-weighted asteroid places mass at the edges.

Though these general trends in mass placement arrived at by both the likelihood and harmonic models are accurate, the precise density distributions are inaccurate because they predict negative densities. This might be addressed for the likelihood model by selecting a likelihood that strongly disfavours negative densities, such as a log-normal distribution. A log-normal likelihood however would no longer yield a linear model, so we do not use one here.

Figure 17 shows that the lumpy model places one large lump of greater density than the surrounding medium for the centre-weighted asteroid and less density for the edge-weighted asteroid, as expected. Greater error is incurred in ΔK_{lm} in this lumpy model than for the harmonic and likelihood models due to the lumpy model's crudeness, but the lump gives a good qualitative estimate of the density distribution of the asteroid which is useful for interpreting the other two models. This fact demonstrates that it can be illustrative to run the models with reduced degrees of freedom

for the sake of simplicity, even if doing so yields less accurate distributions.

The lumpy model has one caveat that has not yet been mentioned, which applies for $N = d = 1$ if (1) the centre of mass of the asteroid is the centroid of the asteroid shape and (2) the density moments of the asteroid shape are proportional to the fitted density moments. (1) guarantees that the lump will be placed at the origin and therefore will not contribute to K_{lm} for $\ell \geq 1$, and (2) guarantees that the mass of the asteroid shape will be chosen such that the shape density moments exactly match the fitted density moments. The lump radius will then be set to zero because the fitted density moments are already matched. This zero-radius-lump result will occur even if the true density distribution has a large-radius lump at the origin. The lump model will therefore fail to recognize the lump in the true density distribution.

An example of this caveat applied is an elliptical lump inside an elliptical asteroid similar to the ones above. This is why, in the centre-weighted and edge-weighted density distributions, we specifically chose a spherically symmetric density distribution for our ellipsoidal asteroid shape, rather than an a distribution that conforms to the asteroid shape.

4.4.4 Lump test

Finally, we test an asteroid with a discrete change in density distribution (for example, a boulder), of the kind that the lumpy model is designed to detect. We place a spherical mass of density six times the density of the surrounding medium inside the asymmetric reference asteroid, slightly displaced along \hat{y} . The rest of the asteroid we set to uniform density.

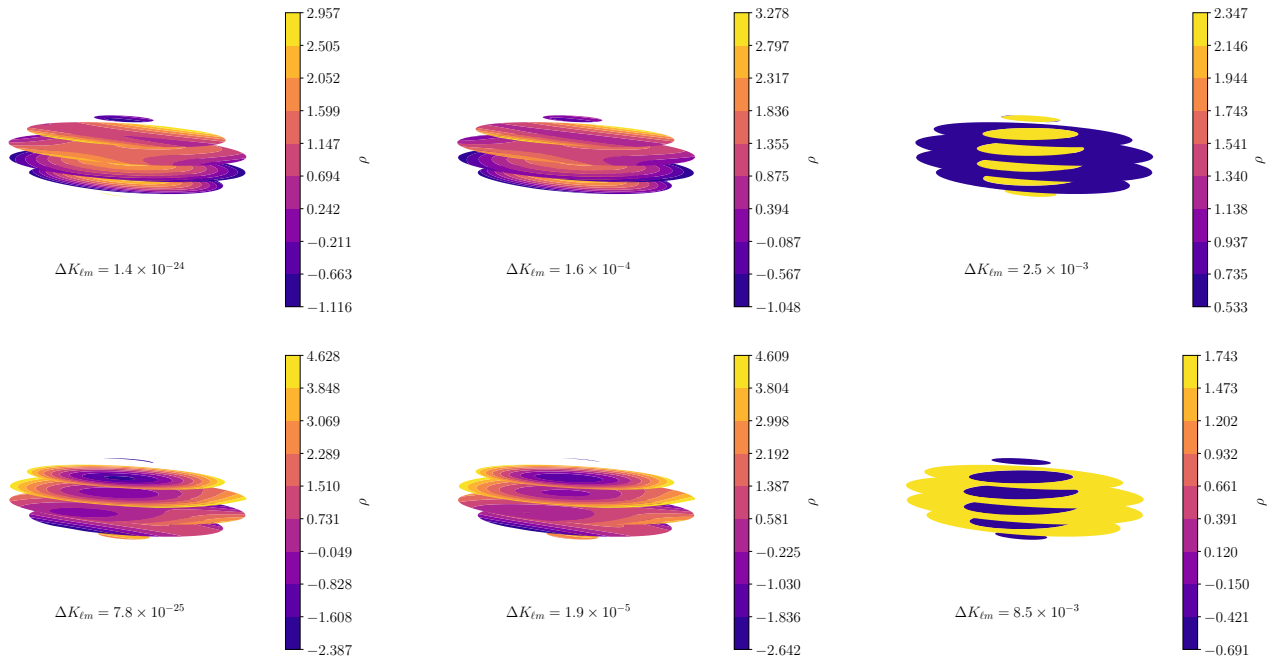


Figure 17. Density distributions extracted by the likelihood (*left*), harmonic (*middle*), and lumpy with $d = N = 1$ (*right*) models from data generated for non-uniform-density asteroids with mass concentrated in the middle (*top*) and the edges (*bottom*). Density is normalized so that mean density is one. The same distance scale is used in all figures.

The density distributions found by the three model for this asteroid are shown in figure 18.

We see from figure 18 that the harmonic and likelihood model fail completely to recover the presence or location of the lump. There appears to be a slight increase in density at roughly the correct location for both models, but this is a small effect. Like figure 17, we see that the harmonic and likelihood models do not agree exactly, and the failure of the harmonic model to exactly reproduce $K_{\ell m}$ suggests that the true distribution is not harmonic.

The failure of these models to find lumps is expected, since $K_{\ell m}$ is most sensitive to non-uniformities of characteristic size $\pi/(\ell + 1)$ radians in the polar direction, and $2\pi/(|m| + 1)$ in the azimuthal direction by the definition of $Y_{\ell m}$. This lump is too small to be resolvable by K_{3m} , so we do not expect most models to find it.

However, the lumpy model computes the location and density of the mass very well. Some inaccuracies are induced by the uncertainty in K_{3m} , which changes the minimum of equation 20 such that the lump is displaced by 9 m along $\hat{\mathbf{y}}$ from where it should be. This in turn causes a 70 m inaccuracy in the lump's radius. Nevertheless, the accuracy is still good compared to other models, and we conclude that the lumpy model is capable of recreating the location of lumps (except for the caveat mentioned in the previous section for distributions with $K_{\ell m}$ proportional to the asteroid shape's moments). But the ability of the lumpy model to place a lump does not guarantee the lump to actually exist, as was seen in the other asteroid distributions analysed here.

5 CONCLUSIONS

We assess the feasibility of extracting density moments and density distributions for a general asteroid encounter, and ask what encounter properties are necessary to obtain the most information about asteroid density.

We derived a novel, arbitrary-order equation for the tidal torque experienced by an asteroid during an encounter with a planet of arbitrary shape and mass distribution. The tidal torque equation (equation 3) revealed that the rotational velocity of the asteroid over time depends strongly on $K_{\ell m}$ and the initial orientation.

We built a fast simulation for an asteroid encounter, truncating the equation at second-order, and used the simulation to extract first- and second-order density moments from synthetic spin pole data via a Markov Chain Monte Carlo fit. We observe the following general properties of the moments:

- (i) The second-order moments K_{3m} are generally a factor of $\frac{a_A}{r_p}$ more uncertain than the first-order moments, where a_A is the asteroid radius and r_p is the perigee distance. For our reference asteroid, this fraction was about 10^{-5} .
- (ii) Of the seven second-order moments, those that measure small-scale variations in density (i.e., $|m|$ is large) are generally less uncertain. It is often possible to measure $K_{3|m|}$ for large m even when K_{30} is not resolved.
- (iii) The oblateness of the central body cannot be ignored without generating incorrect density moment estimates, but a non-zero oblateness does not greatly increase the precision of the extracted moments except perhaps when a moon is present.

We assessed the posterior uncertainty generated by the

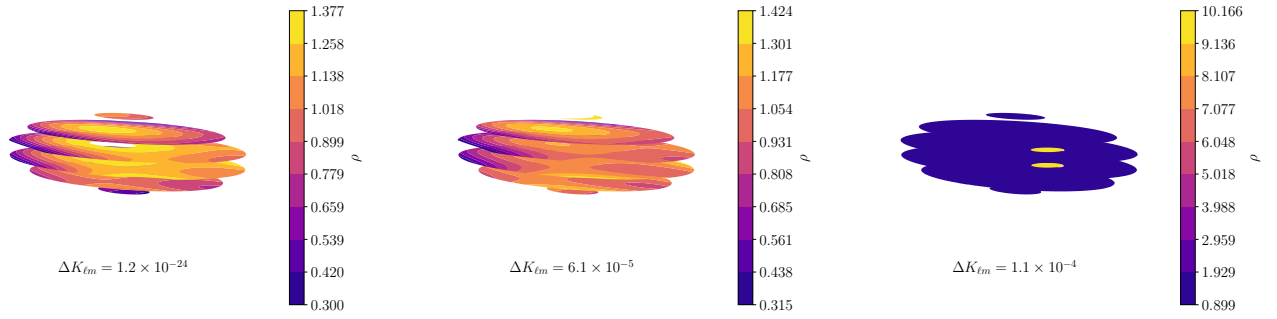


Figure 18. Density distributions extracted by the likelihood (*left*), harmonic (*middle*), and lumpy with $d = N = 1$ (*right*) models from data generated for an asteroid with an off-centre lump. Density is normalized so that mean density is one. The same distance scale is used in all figures.

fit process by adjusting eleven parameters of an asteroid on an Earth encounter. The main conclusions are listed below.

(i) Highly precise rotational velocity data is required to produce precise second-order moments. Especially the uncertainty on the asteroid rotational period must be small compared to the uncertainty on asteroid spin pole.

(ii) Large a_A is required for K_{3m} resolution, though the size of a_A has no effect on K_{2m} . The threshold on a_A for the reference asteroid was ~ 700 m for K_{30} and ~ 50 m for K_{33} .

(iii) A close encounter is vital for accurate second-order moment extraction, though some of the second-order moments can still be required for more distant encounters, extending to about a third of a Lunar distance for the reference asteroid.

(iv) This model will yield inflated uncertainties if the asteroid is rotationally symmetric around its rotating spin axis. In this case, a different parametrization should be used.

(v) If the asteroid rotational period is too small, the asteroid will not tumble after perigee. This inhibits the precise determination of K_{2m} , though K_{3m} are largely unaffected. For the reference asteroid, the threshold was about 4 hours (although K_{30} will become unresolved at for periods smaller than 8 hours). For similar reasons, initial rotational velocities orthogonal to the orbital plane or in the plane and perpendicular to the perigee vector will yield poor-quality fits, though the spin pole effect is smaller than the effect of rotational period.

(vi) The cadence of observation should be shorter than about 30 minutes (except K_{30} will become unresolved for cadence longer than 10 minutes). Gaps of data can appear, specifically at perigee, but only for a little over an hour given 2 minute cadence before the posterior uncertainty greatly increases.

If some of these conditions are not met, the first-order K_{2m} moments may still be resolvable.

Finally, we present three fast, linear methods for extracting density distributions (together with uncertainties) from the density moments and the shape of the asteroid as obtained by light-curve analysis. The extracted density distributions largely are consistent with the true distributions in all cases we tested. Slight adjustments to K_{3m} dramatically change the overall distribution, so that they are not very precise. Indeed, the models sometimes predict negative

density (though more complicated models could be made not to). Errors in the shape estimate of the asteroid also distort the density distribution, but the resulting distributions provide hints as to exactly where the shape is incorrect. Large-scale properties of the asteroid's true distribution, such as whether the mass is located in the middle or on the edges, are often observable. Two of the models presented (the harmonic and lumpy models) are flexible in their number of parameters, so that if only these large-scale properties are necessary, a small set of parameters can be chosen to prevent over-fitting.

In the appendices, we answer more specific questions that might arise about the behaviour of the tidal torque system and the fit process.

ACKNOWLEDGEMENTS

We warmly thank Emmanuel Jehin, Maxime Devogele, and Marin Ferrais for meeting with the authors to discuss this work, and pointing out possible future directions to take it. JTD would like to thank the Massachusetts Institute of Technology Undergraduate Research Opportunities Program (MIT UROP) office for funding his work for many semesters, and their flexibility in funding students from departments other than the source of funding. Much of the computation behind this paper was executed on MIT Supercloud's facilities.

DATA AVAILABILITY

The code used to generate data, fit density moments to it, and extract density distributions from the moments is available on [GitHub](#), or by contacting JTD.

REFERENCES

- Ashenbergs J., 2007, *Celestial Mechanics and Dynamical Astronomy*, 99, 149
- Benson C. J., Scheeres D. J., Moskovitz N. A., 2020, *Icarus*, 340, 113518
- Boué G., Laskar J., 2009, *Icarus*, 201, 750

- Foreman-Mackey D., Hogg D. W., Lang D., Goodman J., 2013, Publications of the Astronomical Society of the Pacific, 125, 306
- Gao F., Han L., 2012, *Computational Optimization and Applications*, 51, 259
- Hirabayashi M., Kim Y., Brozović M., 2021, Icarus, 365, 114493
- Hou X., Scheeres D. J., Xin X., Mar 2017, Celestial Mechanics and Dynamical Astronomy, 127, 369
- Kaiser N., et al., 2002, in Survey and Other Telescope Technologies and Discoveries. pp 154–164
- Kwiecinski J. A., Krause A. L., Van Gorder R. A., 2018, *Icarus*, 311, 170
- Larson S., Brownlee J., Hergenrother C., Spahr T., 1998, in Bulletin of the American Astronomical Society. p. 1037
- Lee H.-J., et al., 2022.
- Makarov V. V., Goldin A., Tkachenko A. V., Veras D., Noyelles B., 2022.
- Moskovitz N. A., et al., 2020, *Icarus*, 340, 113519
- Naidu S. P., Margot J.-L., 2015, *The Astronomical Journal*, 149, 80
- Pater D. I., Lissauer J. J., 2015, Planetary sciences, 2 edn. Cambridge University Press
- Paul M. K., 1988, *Celestial mechanics*, 44, 49
- Richardson D. C., Bottke W. F., Love S. G., 1998, *Icarus*, 134, 47
- Scheeres D., Ostro S., Werner R., Asphaug E., Hudson R., 2000, *Icarus*, 147, 106
- Scheeres D. J., Marzari F., Rossi A., 2004, Icarus, 170, 312
- Souchay J., Souami D., Lhotka C., Puente V., Folgueira M., 2014, *Astronomy & Astrophysics*, 563, A24
- Souchay J., Lhotka C., Heron G., Herve Y., Puente V., Lopez M. F., 2018, *Astronomy & Astrophysics*, 617, A74
- Stokes G. H., Evans J. B., Viggh H. E., Shelly F. C., Pearce E. C., 2000, *Icarus*, 148, 21
- Valvano G., Winter O. C., Sfair R., Machado Oliveira R., Borderes-Motta G., Moura T., 2022, *Monthly Notices of the Royal Astronomical Society*, 510, 95
- Wright E. L., et al., 2010, *The Astronomical Journal*, 140, 1868
- Yu Y., Richardson D. C., Michel P., Schwartz S. R., Ballouz R.-L., 2014, *Icarus*, 242, 82
- van Gelderen M., 1998, in The shift operators and translations of spherical harmonics.

This paper has been typeset from a *T_EX/L_AT_EX* file prepared by the author.